

Structure Formation in Modified Gravity Scenarios

Philippe Brax and Patrick Valageas

Institut de Physique Théorique,

CEA, IPhT, F-91191 Gif-sur-Yvette, Cédex, France

CNRS, URA 2306, F-91191 Gif-sur-Yvette, Cédex, France

(Dated: May 3, 2019)

We study the growth of structures in modified gravity models where the Poisson equation and the relationship between the two Newtonian potentials are modified by explicit functions of space and time. This parameterisation applies to the $f(R)$ models and more generally to screened modified gravity models. We investigate the linear and weakly nonlinear regimes using the “standard” perturbative approach and a resummation technique, while we use the spherical dynamics to go beyond low-order results. This allows us to estimate the matter density power spectrum and bispectrum from linear to highly nonlinear scales, the full probability distribution of the density contrast on weakly nonlinear scales, and the halo mass function. We analyse the impact of modifications of gravity on these quantities for a few realistic models. In particular, we find that the standard one-loop perturbative approach is not sufficiently accurate to probe these effects on the power spectrum and it is necessary to use resummation methods even on weakly nonlinear scales which provide the best observational window for modified gravity as relative deviations from General Relativity do not grow significantly on smaller scales where theoretical predictions become increasingly difficult.

PACS numbers: 98.80.-k

I. INTRODUCTION

The discovery of the acceleration of the expansion of the Universe cannot be explained using General Relativity and a matter content comprising only fluids with a positive equation of state. Seemingly, a new fluid with a negative equation of state, either a cosmological constant or dynamical dark energy, is required to generate the late time acceleration[1]. Another plausible explanation could be that gravity itself is poorly understood on large scales and needs to be modified[2]. As General Relativity (GR) is the unique Lorentz invariant low energy theory of spin two gravitons, any modification of gravity must include new degrees of freedom[3]. Hence, in both the dark energy and the modified gravity contexts, new fields need to be included, the simplest ones being of course scalar fields. However, the presence of scalar fields is tightly constrained by fifth force and equivalence principle tests[4, 5]. This implies that the scalars leading to either dark energy or modified gravity must be screened in local and dense environments such as on earth or in the solar system[6]. Such models abound: chameleons[7–9], dilatons[10–12], Galileons[13], symmetrons[14–16] and their generalisations[17]. In all these cases, the background cosmology coincides with a Λ Cold Dark Matter (Λ CDM) Universe. The only hope of observing non-trivial effects relies on the fact that perturbations in these models grow anomalously inside the Compton radius of the scalar field as first noticed in [9, 18]. This anomalous growth can only be effective on intermediate scales. Indeed, on very large scales outside the Compton radius, normal gravity is retrieved while screening effects imply that GR is also recovered on small scales in very dense regions of the Universe[7]. This opens up the possibility that relevant effects may be present at the mega parsec

scale and that deviations from GR may be detectable by future galaxy surveys.

In the following, we will concentrate on a formulation of the perturbation equations involving two Newtonian potentials and a time and scale dependent relationship between them. In terms of scalar field models, this corresponds to the Jordan frame picture; the difference between the two Newtonian potentials being due to the scalar field perturbation. In this picture, we choose to capture the modified gravity effects using a single function $\epsilon(k, a)$ whose interpretation in the Einstein frame is obvious: it measures the deviations of the geodesics under the influence of the scalar field. This function is universally characterised in terms of the mass and the coupling function of the scalar field. Here, we will consider it as defining the modified gravity models which we will study.

Doing so, we neglect the nonlinear effects due to the presence of non-linear terms originating from the scalar field modifying gravity. As such we only modify the Euler equation by including the effects of a new scalar force. Hence, at this level of approximation, the models only differ from the GR treatment of Λ CDM perturbations by the inclusion of a time and scale dependent contribution to Newton’s constant in the Euler equation. This simple modification of gravity is amenable to a quasi-linear and a fully non-linear treatment.

The precision that future galaxy surveys will reach implies that simple linear perturbation theory is not accurate enough. One must include higher order effects and at one-loop order (i.e., next-to-leading order) we will find that the “standard” perturbative expansion is not sufficiently accurate to probe the modified gravity effects we investigate here. Therefore, we generalise a method derived using the saddle point of the generating functional of matter and velocity fluctuations. This resummation

scheme was already tested in the GR case and shown to be more accurate than the standard approach.

To go beyond these low-order results we also study the dynamics of spherical perturbations. This can be exactly solved until shell crossing and it provides the full probability distribution of the matter density contrast on weakly nonlinear scales as well as the large-mass tail of the halo mass function. The latter can then be used to build a phenomenological halo model that also converges to the perturbative results on quasi-linear scales. This provides a simple estimate of the matter density power spectrum and bispectrum from linear to highly nonlinear scales, and a global picture of structure formation in such modified-gravity scenarios. We discuss the relative deviations from GR of these various quantities as a function of scale.

However, let us note that the analytical treatment of modified gravity developed here should only be taken as a first step, to indicate the type of effects one may expect, because of our simplified parameterization of modified gravity. First, more accurate modelizations would include some of the non-linearities due to the scalar potential at the one loop level[19], which modify the Euler equation in an effective way. Second, the screening effects of the scalar field force in dense regions would modify the spherical collapse of an initial over density[20, 21]. Here and as a first step, we will not consider these issues and treat the modification of gravity at the linear level in the scalar sector of the models. In [22–24], this corresponds to the “non-chameleon” regime which should be seen as a non-screening case here in as much as we are neglecting the screening effects of modified gravity in dense regions. Of course, in future work, we intend to include one-loop corrections in the scalar sector as well as screening effects in the spherical collapse. Yet, it is useful to first develop the analytic formalism for the simpler parameterization studied in this paper. This will serve as a basis for more complex models that involve further ingredients (which are also more model-dependent, while the formalism developed here can be applied to any function $\epsilon(k, a)$ in the Euler equation).

The paper is arranged as follows. In section II, we describe the modified gravity models we will consider. We present the dynamical equations in the hydrodynamical approximation in section III, and we study the perturbative regime in section IV, for the density power spectrum and bispectrum. Next, we analyse the spherical collapse in the no-screening case in section V. This allows us to obtain the probability distribution of the density contrast on weakly nonlinear scales in section VI and the halo mass function in section VII. Finally, we use these ingredients to build a phenomenological halo model in section VIII, which provides estimates of the power spectrum and bispectrum from linear to highly nonlinear scales. We conclude in section IX.

II. MODIFIED GRAVITY

A. The perturbed equations

We consider models of modified gravity which can be defined by a change of the perturbation equations for Cold Dark Matter (CDM). The modifications are usually parameterised by two time and scale dependent functions $\gamma(k, a)$ and $\mu(k, a)$. This parameterisation does not follow directly from a Lagrangian formulation where causality is automatically taken into account. In the following, we will use a restricted class of modified gravity models where the perturbed dynamics can be entirely specified by two time dependent functions only, $m(a)$ and $\beta(a)$. These two functions enter as building blocks of a time and space dependent function $\epsilon(k, a)$. Finally, the knowledge of $\epsilon(k, a)$ defines $\gamma(k, a)$ and $\mu(k, a)$ completely. The origin of this parameterisation springs from modified gravity models where a scalar field alters gravity on large scales and is screened in dense environments, leading to no modification of gravity in the solar system and in laboratory experiments. In turn, the dynamics of these models can be entirely reconstructed from the time evolution of the mass function $m(a)$ of the scalar field, and its coupling to matter particles $\beta(a)$. This way of describing modifying gravity applies to chameleons and $f(R)$ models, symmetrons and dilatons. Here, we will simply use the $\{m(a), \beta(a)\}$ parameterisation as a way of unambiguously defining modified gravity models at the level of the perturbations.

At the linear level, the perturbation equations of the CDM fluid follow from the conservation of matter

$$\theta = -\delta', \quad (1)$$

where the density contrast is $\delta = (\rho_m - \bar{\rho}_m)/\bar{\rho}_m$ and $\theta = \partial^i v_i$ is the divergence of the velocity field. We denote by a prime the time derivative in conformal time τ , with $d\tau = dt/a$ and $a(t)$ is the scale factor. The Euler equation involves the Newtonian potential Ψ and reads in Fourier space as

$$\tilde{\theta}' + \mathcal{H}\tilde{\theta} = k^2\tilde{\Psi}, \quad (2)$$

where we denote Fourier-space quantities with a tilde. Here $\mathcal{H} = a'/a$ is the conformal expansion rate and we are using the Newtonian gauge with two distinct potentials Ψ and Φ ,

$$ds^2 = -a^2(1 + 2\Psi)d\tau^2 + a^2(1 - 2\Phi)d\mathbf{x}^2, \quad (3)$$

where \mathbf{x} are comoving coordinates. The gravitational dynamics determine the evolution of Φ as

$$-k^2\tilde{\Phi} = 4\pi\nu(k, a)\mathcal{G}\bar{\rho}_m\tilde{\delta}/a, \quad (4)$$

which is a modification of the Poisson equation ($\bar{\rho}_m$ is the mean comoving matter density and \mathcal{G} is Newton's constant). We also assume that there is a constitutional relation between the two potentials,

$$\tilde{\Psi} = \gamma(k, a)\tilde{\Phi}, \quad (5)$$

implying that

$$-k^2\tilde{\Psi} = 4\pi\mu(k, a)\mathcal{G}\bar{\rho}_m\tilde{\delta}/a, \quad (6)$$

where

$$\mu(k, a) = \gamma(k, a)\nu(k, a). \quad (7)$$

As a result, this implies that the density contrast obeys

$$\tilde{\delta}'' + \mathcal{H}\tilde{\delta}' - \frac{3\Omega_m}{2}\mathcal{H}^2\mu(k, a)\tilde{\delta} = 0, \quad (8)$$

where $\Omega_m(a)$ is the matter density cosmological parameter. The growth of structures depends on the choice of the function $\mu(k, a)$. We will define a large class of such models in the following section.

B. Parameterised modified gravity

The choice of function $\mu(k, a)$ seems to be unlimited. Here we focus on the simple choice

$$\mu(k, a) = 1 + \epsilon(k, a) \quad (9)$$

and

$$\gamma(k, a) = \frac{1 + \epsilon(k, a)}{1 - \epsilon(k, a)}, \quad (10)$$

where ϵ measures the deviation from General Relativity and is defined by two time dependent functions only, $m(a)$ and $\beta(a)$ [17]. In modified gravity models with a screened scalar field in dense environments, $m(a)$ is the mass of the scalar field at the cosmological background level. Similarly $\beta(a)$ is the coupling function between the scalar field and CDM particles. The space and time dependent function $\epsilon(k, a)$ is expressed as

$$\epsilon(k, a) = \frac{2\beta^2(a)}{1 + \frac{m^2(a)a^2}{k^2}} \quad (11)$$

This parameterisation is valid for chameleons and $f(R)$ models, symmetrons and dilatons[17]. This implies in particular that

$$\mu(k, a) = \frac{(1 + 2\beta^2)k^2 + m^2a^2}{k^2 + m^2a^2} \quad (12)$$

and

$$\gamma(k, a) = \frac{(1 + 2\beta^2)k^2 + m^2a^2}{(1 - 2\beta^2)k^2 + m^2a^2}. \quad (13)$$

This is an explicit parametrisation which shows that modified gravity effects only appear on scales such that $k \gtrsim am(a)$, i.e. when scales are within the Compton wavelength of the scalar field. Outside the Compton wavelength, General Relativity is retrieved.

In the rest of this paper, we will only deal with one particular family of models defined by the coupling constant

$$\beta = \frac{1}{\sqrt{6}} \quad (14)$$

and the mass of the scalar field which is given by

$$m(a) = m_0 a^{-3(n+2)/2}, \quad (15)$$

where m_0 is a free scale which will be chosen to be close to 1 Mpc^{-1} and $n > 0$. In the matter dominated epoch, these models are equivalent to $f(R)$ theories in the large curvature regime[17] where the $f(R)$ correction to the Einstein-Hilbert action reads[25]

$$f(R) \approx -16\pi\mathcal{G}\rho_\Lambda - \frac{f_{R_0}}{n} \frac{R_0^{1+n}}{R^n} \quad (16)$$

and ρ_Λ is the effective dark energy in the late time Universe. In the recent past of the Universe, the mass of the large curvature models differs slightly from (15), see the appendix for more details. The mass m_0 is given by the useful relationship

$$m_0 = \frac{H_0}{c} \sqrt{\frac{\Omega_{m0} + 4\Omega_{\Lambda0}}{(n+1)|f_{R0}|}} \quad (17)$$

with $c/H_0 \approx 4 \text{ Gpc}$. Modifications of gravity must satisfy $m_0 c/H_0 \gtrsim 10^3$ to comply with a loosely screened Milky Way [26]. This also corresponds to $|f_{R0}|$ less than 10^{-5} , the case $|f_{R0}| = 10^{-4}$ being marginal. When m_0 is too large, effects of modified gravity on large scale structure occur on very non-linear scales. In the following, we will use values of $m_0 \sim 1 \text{ Mpc}^{-1}$ which satisfy the loose screening bound for the Milky Way and imply interesting effects on large scale structure.

We can also deduce now the two parametric functions

$$\mu(k, a) = \frac{\frac{4}{3} \frac{k^2}{m_0^2} a^s + 1}{\frac{k^2}{m_0^2} a^s + 1} \quad (18)$$

and

$$\gamma(k, a) = \frac{\frac{4}{3} \frac{k^2}{m_0^2} a^s + 1}{\frac{2}{3} \frac{k^2}{m_0^2} a^s + 1}, \quad (19)$$

where

$$s = 3n + 4. \quad (20)$$

We will use the parameterisation of $\epsilon(k, a)$ in the following when we give numerical examples. More precisely, we will consider the four cases $(n, m_0) = (0, 0.1), (0, 1), (1, 0.1)$, and $(1, 1)$, where m_0 is given in units of Mpc^{-1} . This corresponds to the two scales $m_0 = 0.1$ and 1 Mpc^{-1} and to the two exponents $n = 0$ and 1 . For these models we should have $n > 0$, see

Eq.(16), and the choice $n = 0$ for our numerical computations is only meant to exemplify the case of small n , that is $s \rightarrow 4$. The scales we consider are of the same order as the ones used so far in N-body simulations where $|f_{R0}| = 10^{-4}, 10^{-5}, 10^{-6}$ and $n = 1$. We will give a qualitative comparison with these numerical results, especially we will briefly analyse the difference between the full numerical simulations, the no-chameleon case where the chameleon effects in dense region is neglected and our resummation method in the appendix. There we analyse the $f(R)$ models where we take into account the late time effect of the cosmological constant on the mass function $m(a)$. A more quantitative comparison is left for future work.

III. PERTURBATIVE DYNAMICS

A. Hydrodynamical perturbations

As explained in the previous section and in the introduction, we consider models where the continuity and the Euler equations are only modified by the non-trivial relationship between the two Newtonian potentials. Formally, these equations have the same structure as in GR. When interpreted in terms of scalar field models, new non-linearities should appear in the Euler equation. However, the analysis of their role is left for future work. Then, the continuity and Euler equations read in Fourier space as

$$\frac{\partial \tilde{\delta}}{\partial \tau}(\mathbf{k}, \tau) + \tilde{\theta}(\mathbf{k}, \tau) = - \int d\mathbf{k}_1 d\mathbf{k}_2 \delta_D(\mathbf{k}_1 + \mathbf{k}_2 - \mathbf{k}) \times \alpha(\mathbf{k}_1, \mathbf{k}_2) \tilde{\theta}(\mathbf{k}_1, \tau) \tilde{\delta}(\mathbf{k}_2, \tau), \quad (21)$$

$$\begin{aligned} \frac{\partial \tilde{\theta}}{\partial \tau}(\mathbf{k}, \tau) + \mathcal{H} \tilde{\theta}(\mathbf{k}, \tau) + \frac{3\Omega_m}{2} \mathcal{H}^2 [1 + \epsilon(k, \tau)] \tilde{\delta}(\mathbf{k}, \tau) = \\ - \int d\mathbf{k}_1 d\mathbf{k}_2 \delta_D(\mathbf{k}_1 + \mathbf{k}_2 - \mathbf{k}) \beta(\mathbf{k}_1, \mathbf{k}_2) \tilde{\theta}(\mathbf{k}_1, \tau) \tilde{\theta}(\mathbf{k}_2, \tau), \end{aligned} \quad (22)$$

which are the nonlinear generalizations of Eqs.(1) and (2), with the parameterization (9). The kernels α and β are given by

$$\alpha(\mathbf{k}_1, \mathbf{k}_2) = \frac{(\mathbf{k}_1 + \mathbf{k}_2) \cdot \mathbf{k}_1}{k_1^2}, \beta(\mathbf{k}_1, \mathbf{k}_2) = \frac{|\mathbf{k}_1 + \mathbf{k}_2|^2 (\mathbf{k}_1 \cdot \mathbf{k}_2)}{2k_1^2 k_2^2}. \quad (23)$$

In this paper we are mostly interested in the recent Universe on large scales, hence we do not distinguish between the dark matter and the baryons that are treated as usual as a single collisionless fluid. These equations are only a first approximation of the dynamics of modified gravity on sub-horizon scales. Indeed, non-linearities in the potential and coupling function of the scalar field inducing the modification of gravity imply that the full dynamics

should be described by the fluid equations for CDM particles and the Klein-Gordon equation for the scalar field. Here we consider only the linear part of the scalar field dynamics which is tantamount to treating the scalar field as massive with a linear coupling to matter. When the mass of the scalar field is large enough $m(a) \gg H$, this allows one to integrate out the scalar dynamics and reduce the equations of motion to the previous ones with a modified Newton constant. A priori, this procedure can be carried out to all orders taking into account the higher derivatives of the scalar field potential and coupling function at the minimum of the effective potential describing the background cosmology. Explicitly, this has been carried out to the one-loop level in the scalar field perturbation, resulting in an effective dynamics, once the scalar field effects have been integrated out, with a modified $\beta(\mathbf{k}_1, \mathbf{k}_2)$ [19]. The effect of this new contribution will be taken into account in a forthcoming publication.

It is convenient to write the two fields δ and θ as a two-component vector ψ [27], which we define as

$$\psi \equiv \begin{pmatrix} \psi_1 \\ \psi_2 \end{pmatrix} \equiv \begin{pmatrix} \delta \\ -\theta/\dot{a} \end{pmatrix}. \quad (24)$$

Because of the factor $\epsilon(k, \tau)$ in the Euler equation (22) the linear growing mode $D_+(k, t)$ depends on the wavenumber k . Therefore, instead of using D_+ as the time coordinate we use the logarithm of the scale factor,

$$\eta(t) = \ln a(t). \quad (25)$$

This agrees with the standard choice used in most perturbative studies for the simpler case of the Einstein-de-Sitter universe, where $D_+ = a$ [27–30]. Then, the equations of motion (21)-(22) read as

$$\begin{aligned} \frac{\partial \tilde{\psi}_1}{\partial \eta} - \tilde{\psi}_2 = \int d\mathbf{k}_1 d\mathbf{k}_2 \delta_D(\mathbf{k}_1 + \mathbf{k}_2 - \mathbf{k}) \alpha(\mathbf{k}_1, \mathbf{k}_2) \\ \times \tilde{\psi}_2(\mathbf{k}_1) \tilde{\psi}_1(\mathbf{k}_2), \end{aligned} \quad (26)$$

$$\begin{aligned} \frac{\partial \tilde{\psi}_2}{\partial \eta} - \frac{3}{2} \Omega_m (1 + \epsilon) \tilde{\psi}_1 + \left(\frac{1}{2} - \frac{3}{2} w \Omega_{de} \right) \tilde{\psi}_2 = \\ \int d\mathbf{k}_1 d\mathbf{k}_2 \delta_D(\mathbf{k}_1 + \mathbf{k}_2 - \mathbf{k}) \beta(\mathbf{k}_1, \mathbf{k}_2) \tilde{\psi}_2(\mathbf{k}_1) \tilde{\psi}_2(\mathbf{k}_2), \end{aligned} \quad (27)$$

where $\Omega_{de}(a)$ is the dark energy cosmological parameter and w the dark energy equation-of-state parameter. As in [28, 31, 32], this can be written in a more concise form as

$$\mathcal{O}(x, x') \cdot \tilde{\psi}(x') = K_s(x; x_1, x_2) \cdot \tilde{\psi}(x_1) \tilde{\psi}(x_2), \quad (28)$$

where we have introduced the coordinate $x = (\mathbf{k}, \eta, i)$, $i = 1, 2$ is the discrete index of the two-component vector $\tilde{\psi}$, and repeated coordinates are integrated over. The matrix \mathcal{O} reads as

$$\begin{aligned} \mathcal{O}(x, x') = \delta_D(\mathbf{k} - \mathbf{k}') \delta_D(\eta - \eta') \\ \times \begin{pmatrix} \frac{\partial}{\partial \eta} & -1 \\ -\frac{3}{2} \Omega_m(\eta)(1 + \epsilon(k, \eta)) \frac{\partial}{\partial \eta} + \frac{1}{2} - \frac{3}{2} w \Omega_{de}(\eta) \end{pmatrix} \end{aligned} \quad (29)$$

and the symmetric vertex K_s is

$$K_s(x; x_1, x_2) = \delta_D(\mathbf{k}_1 + \mathbf{k}_2 - \mathbf{k}) \delta_D(\eta_1 - \eta) \delta_D(\eta_2 - \eta) \times \gamma_{i; i_1, i_2}^s(\mathbf{k}_1, \mathbf{k}_2), \quad (30)$$

with

$$\gamma_{1;1,2}^s(\mathbf{k}_1, \mathbf{k}_2) = \frac{\alpha(\mathbf{k}_2, \mathbf{k}_1)}{2}, \quad \gamma_{1;2,1}^s(\mathbf{k}_1, \mathbf{k}_2) = \frac{\alpha(\mathbf{k}_1, \mathbf{k}_2)}{2},$$

$$\gamma_{2;2,2}^s(\mathbf{k}_1, \mathbf{k}_2) = \beta(\mathbf{k}_1, \mathbf{k}_2), \quad (31)$$

and zero otherwise.

The vertex K_s does not depend on cosmology and it is not modified. Here modified gravity only affects the linear operator \mathcal{O} through the term $\epsilon(k, \eta)$. In the case of a Λ CDM universe, that is, for $\epsilon = 0$, the matrix \mathcal{O} and the linear growing mode $D_+(t)$ only depend on time. Then, it is possible to remove the explicit time-dependence of the equations of motion by using the time-coordinate $\eta = \ln D_+$ and making the approximation $\Omega_m/f^2 \simeq 1$, where $f = d \ln D_+ / d \ln a$. This is a good approximation that is used in most perturbative works and it means that terms of order n in perturbation theory scale with time as $D_+(t)^n$ [33]. Here we do not use this approximation because we consider the case where the linear growing mode and the matrix \mathcal{O} also depend on wavenumber. This also means that in the Λ CDM limit, $\epsilon \rightarrow 0$, our approach is exact in the sense that it does not rely on the approximation $\Omega_m/f^2 \simeq 1$.

B. Linear regime

1. Linear growing and decaying modes

The linear regime corresponds to the linearization of the equations of motion (28) or (26)-(27). We have already discussed the linear equations in section II A to introduce modified-gravity effects. Here we present a more detailed analysis. The linear equations are $\mathcal{O} \cdot \psi_L = 0$ or

$$\frac{\partial \tilde{\psi}_{L1}}{\partial \eta} - \tilde{\psi}_{L2} = 0, \quad (32)$$

$$\frac{\partial \tilde{\psi}_{L2}}{\partial \eta} - \frac{3}{2} \Omega_m (1 + \epsilon) \tilde{\psi}_{L1} + \left(\frac{1}{2} - \frac{3}{2} w \Omega_{de} \right) \tilde{\psi}_{L2} = 0, \quad (33)$$

where the subscript “L” denotes the linear solutions. Substituting Eq.(32) into Eq.(33) yields a second-order equation for the linear modes $D(\eta)$,

$$\frac{\partial^2 D}{\partial \eta^2} + \left(\frac{1}{2} - \frac{3}{2} w \Omega_{de} \right) \frac{\partial D}{\partial \eta} - \frac{3}{2} \Omega_m (1 + \epsilon) D = 0. \quad (34)$$

As usual, we have a growing mode $D_+(\eta)$ and a decaying mode $D_-(\eta)$, and we define the initial conditions by the growing mode D_+ , so that in the linear regime we have:

$$\tilde{\psi}_L(\mathbf{k}, \eta) = \tilde{\delta}_{L0}(\mathbf{k}) \left(\frac{D_+(k, \eta)}{\frac{\partial D_+}{\partial \eta}(k, \eta)} \right). \quad (35)$$

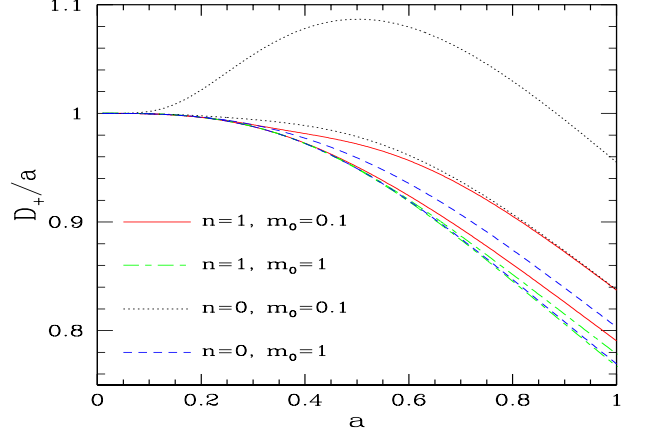


FIG. 1: Linear growing mode $D_+(k, t)$ normalized to the scale factor $a(t)$ for four (n, m_0) models. In each case we show the results for wavenumbers $k = 1 h\text{Mpc}^{-1}$ (lower curve) and $k = 5 h\text{Mpc}^{-1}$ (upper curve), as a function of $a(t)$. These two scales are in the non-linear regime and have only been chosen to exemplify the type of effects obtained in modified gravity.

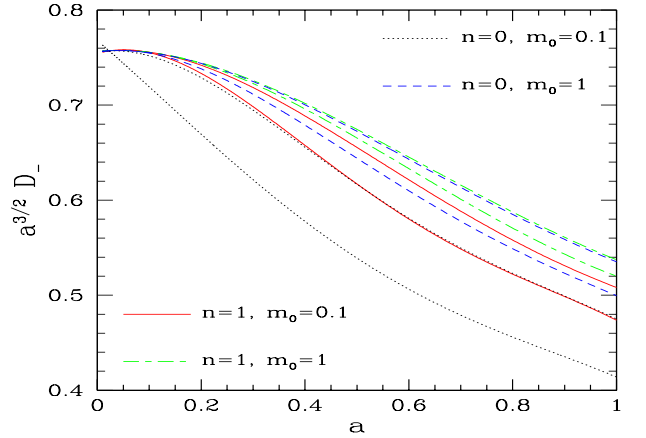


FIG. 2: Linear decaying mode $D_-(k, t)$ normalized to $a(t)^{-3/2}$ for four (n, m_0) models. In each case we show the results for wavenumbers $k = 1 h\text{Mpc}^{-1}$ (upper curve) and $5 h\text{Mpc}^{-1}$ (lower curve), as a function of $a(t)$. These two scales are in the non-linear regime and have only been chosen to exemplify the type of effects obtained in modified gravity.

In other words, we assume the decaying mode has had time to decrease to a negligible amplitude, which is the case in standard cosmologies. Then, the initial conditions are fully determined by the linear density field $\tilde{\delta}_{L0}(\mathbf{k})$.

It is convenient to normalize the growing mode to the scale factor at early times. Indeed, we consider modified-gravity models parameterized by a function $\epsilon(k, a)$ such that $\epsilon \rightarrow 0$ for $a \rightarrow 0$. Then, at early times we recover the Einstein-de Sitter universe (the dark energy component also becomes negligible) and we have the usual be-

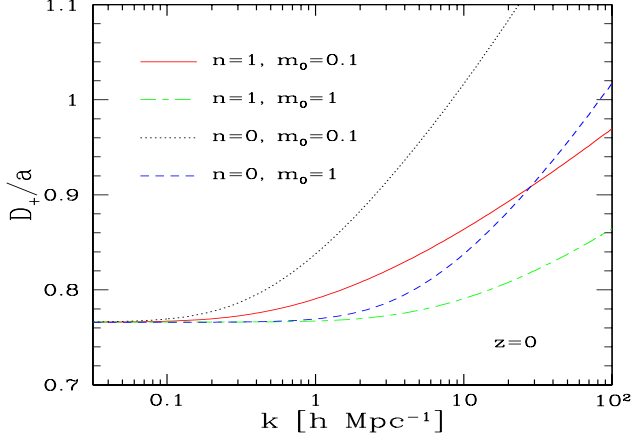


FIG. 3: Linear growing mode $D_+(k, t)$ normalized to the scale factor $a(t)$ for four (n, m_0) models, at redshift $z = 0$ up to non-linear scales.

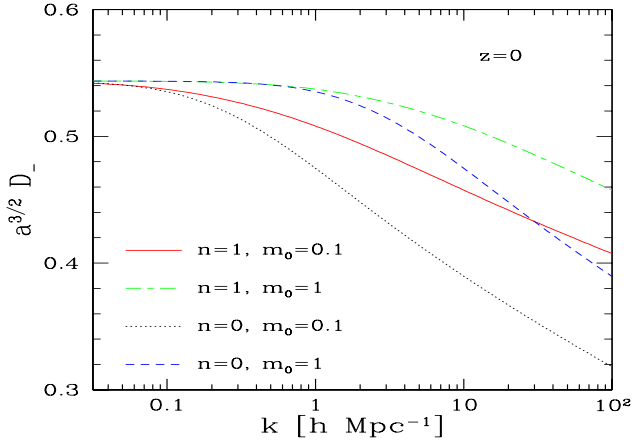


FIG. 4: Linear decaying mode $D_-(k, t)$ normalized to $a(t)^{-3/2}$ for four (n, m_0) models, at redshift $z = 0$ up to non-linear scales.

haviours:

$$t \rightarrow 0: D_+ \rightarrow a = e^\eta, D_- \propto a^{-3/2} = e^{-3\eta/2}. \quad (36)$$

For numerical computations, it is convenient to introduce the reduced growing mode $g_+(k, \eta) = D_+(k, \eta)/a$. From Eq.(34) it obeys

$$\frac{\partial^2 g_+}{\partial \eta^2} + \left(\frac{5}{2} - \frac{3}{2} w \Omega_{\text{de}} \right) \frac{\partial g_+}{\partial \eta} + \frac{3}{2} [(1-w)\Omega_{\text{de}} - \Omega_{\text{m}} \epsilon] g_+ = 0 \quad (37)$$

with the initial conditions

$$\eta \rightarrow -\infty: g_+ \rightarrow 1, \quad \frac{\partial g_+}{\partial \eta} \rightarrow 0. \quad (38)$$

The linear growing mode can be easily computed from Eqs.(37)-(38). Although the linear decaying mode D_-

also obeys Eq.(34) it is not convenient to use this for numerical computations (solving forward in time is unstable because of the contamination by the growing mode). It is better to use the Wronskian,

$$W = D_+ \frac{\partial D_-}{\partial \eta} - \frac{\partial D_+}{\partial \eta} D_-, \quad (39)$$

which in our case is still independent of k and given by

$$W(\eta) = -e^{-(1/2) \int_0^\eta d\eta' [1-3w\Omega_{\text{de}}(\eta')]} \quad (40)$$

This normalization of W also defines the normalization of D_- , which reads

$$D_-(k, \eta) = -D_+(k, \eta) \int_\eta^\infty d\eta' \frac{W(\eta')}{D_+(k, \eta')^2}. \quad (41)$$

The integrals in Eqs.(40) and (41) allow a fast computation of $D_-(k, \eta)$.

We show in Figs. 1 and 2 the linear growing and decaying modes as a function of time (described by the scale factor $a(t)$). The deviation from the General Relativity linear mode (which is almost identical to the lower curve in Fig. 1 and to the upper curve in Fig. 2) increases for higher wavenumber. On these scales, the effects of modified gravity grow as we span the parameters $(n, m_0) = (1, 1), (0, 1), (1, 0.1), (0, 0.1)$. Indeed, as seen from Eqs.(18)-(20), deviations from GR appear at lower k for small mass m_0 and at earlier time for smaller n . We can see that a positive $\epsilon(k, a)$ in the Euler equation (22) leads to a larger growing mode D_+ and a smaller decaying mode D_- . This can be understood from the fact that a positive ϵ can also be interpreted as a larger effective Newton constant in Eq.(6). This implies a faster development of gravitational clustering and both linear modes evolve faster than in the Λ CDM cosmology.

These behaviours can also be seen in Figs. 3 and 4 where we show the linear modes as a function of wavenumber at redshift $z = 0$. Although we plot our results up to $k = 100 h \text{Mpc}^{-1}$ to allow a clear separation between different curves, values beyond $1 h \text{Mpc}^{-1}$ do not describe the true quantitative difference between the models for observables such as the power spectrum because they are in the nonlinear regime, which is not described by these linear modes. In addition, on small scales new “screening” mechanisms, which are not described by the equations of motion (21)-(22), take place and lead to a convergence to General Relativity and to the Λ CDM predictions. In agreement with the parameterization (11), the linear modes deviate from the GR result at a wavenumber $k \sim m_0$ (in the plots the values of m_0 are given in units of 1Mpc^{-1}). At high k the deviation is larger for smaller n (whence smaller s) because modifications of gravity have had more time to affect the dynamics, see Eq.(18).

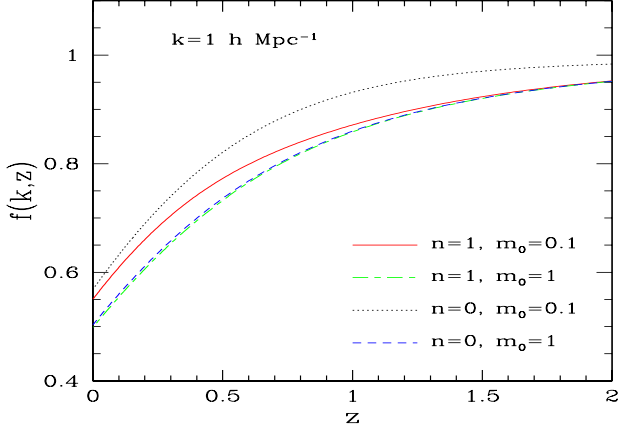


FIG. 5: Linear growth rate $f(k, z) = \partial \ln D_+ / \partial \ln a$ for wavenumber $k = 1 h \text{Mpc}^{-1}$, for four (n, m_0) models.

2. Linear growth rate

We plot in Fig. 5 the linear growth rate $f(k, z)$ as a function of redshift, defined as usual by

$$f(k, z) = \frac{\partial \ln D_+(k, a)}{\partial \ln a}. \quad (42)$$

Both the linear growing mode D_+ and the linear growth rate f depend on wavenumber and to avoid overcrowding the figure we only plot our results for $k = 1 h \text{Mpc}^{-1}$ (which is in the mildly nonlinear regime at $z = 0$). The ΛCDM prediction could not be distinguished from the results obtained for $(n, m_0) = (1, 1)$ and $(0, 1)$ (lower curves). In agreement with Fig. 1, the larger linear growing modes D_+ obtained for $(n, m_0) = (1, 0.1)$ and $(0, 0.1)$ lead to larger growth rates f . The deviation associated with the case $(n, m_0) = (1, 0.1)$ would be difficult to detect with future surveys such as Euclid but the case $(n, m_0) = (0, 0.1)$ should give a clear signal (see Fig. 2.5 in [34]).

3. Linear correlation and response functions

From Eq.(35) the linear two-point correlation of the vector ψ_L , whence of the linear density and velocity fields, reads as

$$C_L(x_1, x_2) = \langle \tilde{\psi}_L(x_1) \tilde{\psi}_L(x_2) \rangle \quad (43)$$

$$= \delta_D(\mathbf{k}_1 + \mathbf{k}_2) P_{L0}(k_1) \begin{pmatrix} D_{+1} D_{+2} & D_{+1} D'_{+2} \\ D'_{+1} D_{+2} & D'_{+1} D'_{+2} \end{pmatrix} \quad (44)$$

where $D_{+i} = D_+(k_i, \eta_i)$ and $D'_{+i} = \frac{\partial D_+}{\partial \eta}(k_i, \eta_i)$.

In Sect. IV B 2 we will consider a perturbative resummation scheme that goes beyond standard one-loop perturbation theory. It involves the response function

(or propagator) defined as the average of the functional derivative

$$R(x_1, x_2) = \left\langle \frac{\mathcal{D}\tilde{\psi}(x_1)}{\mathcal{D}\tilde{\zeta}(x_2)} \right\rangle_{\tilde{\zeta}=0}, \quad (45)$$

where $\tilde{\zeta}$ is a “noise” added to the right hand side of Eq.(28). Thus, $R(x_1, x_2)$ measures the response of the system at time η_1 to an infinitesimal perturbation at an earlier time η_2 . It also describes the “propagation” of infinitesimal fluctuations. By causality, it satisfies

$$\eta_1 < \eta_2 : R(x_1, x_2) = 0, \quad (46)$$

and it obeys the initial condition

$$\eta_1 \rightarrow \eta_2^+ : R(x_1, x_2) \rightarrow \delta_D(\mathbf{k}_1 - \mathbf{k}_2) \delta_{i_1, i_2}. \quad (47)$$

In the linear regime, where the equation of motion (28) reduces to $\mathcal{O} \cdot \psi_L = 0$, the response function obeys

$$\eta_1 > \eta_2 : \mathcal{O} \cdot R_L = 0. \quad (48)$$

Using the initial condition (47), this gives

$$R_L(x_1, x_2) = \frac{\Theta(\eta_1 - \eta_2) \delta_D(\mathbf{k}_1 - \mathbf{k}_2)}{D'_{+2} D_{-2} - D_{+2} D'_{-2}} \times \begin{pmatrix} D'_{+2} D_{-1} - D'_{-2} D_{+1} & D_{-2} D_{+1} - D_{+2} D_{-1} \\ D'_{+2} D'_{-1} - D'_{-2} D'_{+1} & D_{-2} D'_{+1} - D_{+2} D'_{-1} \end{pmatrix} \quad (49)$$

which involves both the linear growing and decaying modes D_+ and D_- . Here $\Theta(\eta_1 - \eta_2)$ is the Heaviside function, which ensures causality.

IV. PERTURBATIVE REGIME

The equation of motion (28) is nonlinear and it has no explicit general solution. Therefore, it is usually solved by perturbative methods, which are sufficient on large scales and at early times where the density and velocity fluctuations are small. Within our parameterization, modified gravity only changes the linear operator \mathcal{O} of Eq.(29), through the factor $\epsilon(k, \eta)$. Thus, we keep the same quadratic nonlinearity as in General Relativity, with the same vertex K_s of Eq.(30). Therefore, we can use the same perturbative schemes as in standard cosmologies.

We first describe the standard perturbative approach in Sect. IV A and next a more accurate resummation scheme in Sect. IV B 2. Here we only go up to “one-loop order”: our standard perturbative prediction only includes the linear and one-loop (i.e., next-to-leading) terms, while our resummed prediction only adds a partial resummation of higher-order terms.

We follow the approach described in detail in [35] (see also [28, 31]).

A. Standard expansion

Since the equation of motion (28) is quadratic in $\tilde{\psi}$, it can be solved through a perturbative expansion in powers of the linear solution $\tilde{\psi}_L$, as

$$\tilde{\psi}(x) = \sum_{n=1}^{\infty} \tilde{\psi}^{(n)}(x), \quad \text{with } \tilde{\psi}^{(n)} \propto (\tilde{\psi}_L)^n. \quad (50)$$

Substituting this expansion into Eq.(28) gives the recursion

$$\mathcal{O} \cdot \tilde{\psi}^{(n)} = K_s(x; x_1, x_2) \cdot \sum_{\ell=1}^{n-1} \tilde{\psi}^{(\ell)}(x_1) \tilde{\psi}^{(n-\ell)}(x_2), \quad (51)$$

which allows to compute terms of increasing order, starting with $\tilde{\psi}^{(1)} = \tilde{\psi}_L$. One usually writes the expansion (50) in terms of the density and velocity fields, as [33, 36]

$$\begin{aligned} \tilde{\delta}(\mathbf{k}, \eta) &= \sum_{n=1}^{\infty} \int d\mathbf{k}_1 \dots \mathbf{k}_n \delta_D(\mathbf{k}_1 + \dots + \mathbf{k}_n - \mathbf{k}) \\ &\times F_n^s(\mathbf{k}_1, \dots, \mathbf{k}_n; \eta) \tilde{\delta}_{L0}(\mathbf{k}_1) \dots \tilde{\delta}_{L0}(\mathbf{k}_n), \end{aligned} \quad (52)$$

and

$$\begin{aligned} \tilde{\theta}(\mathbf{k}, \eta) &= \sum_{n=1}^{\infty} \int d\mathbf{k}_1 \dots \mathbf{k}_n \delta_D(\mathbf{k}_1 + \dots + \mathbf{k}_n - \mathbf{k}) \\ &\times E_n^s(\mathbf{k}_1, \dots, \mathbf{k}_n; \eta) \tilde{\delta}_{L0}(\mathbf{k}_1) \dots \tilde{\delta}_{L0}(\mathbf{k}_n), \end{aligned} \quad (53)$$

where $\tilde{\delta}_{L0}$ is the linear density field at some chosen time, as in Eq.(35). The symmetrized kernels F_n^s and E_n^s are obtained from the recursion (51). In General Relativity the time-dependence of these kernels factorizes as $F_n^s \propto D_+^n F_n^s(\mathbf{k}_1, \dots, \mathbf{k}_n)$ and $E_n^s \propto -a(d \ln D_+ / dt) D_+^n E_n^s(\mathbf{k}_1, \dots, \mathbf{k}_n)$ upon using the approximation $\Omega_m / f^2 \simeq 1$ [33]. In our case, where the linear growing mode $D_+(k, \eta)$ depends on wavenumber, there is no such factorization and one must solve for the kernels $F_n^s(\mathbf{k}_1, \dots, \mathbf{k}_n; \eta)$ and $E_n^s(\mathbf{k}_1, \dots, \mathbf{k}_n; \eta)$ for each time η of interest.

Finally, from the expansion (50) one obtains the two-point correlation as

$$C(x_1, x_2) = \langle \tilde{\psi}(x_1) \tilde{\psi}(x_2) \rangle \quad (54)$$

$$\begin{aligned} &= \langle \tilde{\psi}^{(1)} \tilde{\psi}^{(1)} \rangle + \langle \tilde{\psi}^{(3)} \tilde{\psi}^{(1)} \rangle + \langle \tilde{\psi}^{(1)} \tilde{\psi}^{(3)} \rangle \\ &+ \langle \tilde{\psi}^{(2)} \tilde{\psi}^{(2)} \rangle + \dots \end{aligned} \quad (55)$$

where we can use Wick's theorem to perform the average over the initial conditions $\tilde{\psi}_{L0}$. In particular, up to one-loop order the density power spectrum reads as

$$P(k, \eta) = P^{\text{tree}}(k, \eta) + P^{\text{1loop}}(k, \eta), \quad (56)$$

where P^{tree} , associated with “tree diagrams”, also corresponds to the linear power spectrum,

$$P^{\text{tree}}(k, \eta) = P_L(k, \eta) = D_+(k, \eta)^2 P_{L0}(k), \quad (57)$$

while P^{1loop} , associated with “one-loop” diagrams, is also given by

$$P^{\text{1loop}}(k, \eta) = P^{(b)}(k, \eta) + P^{(c)}(k, \eta), \quad (58)$$

using the notations of [35], with (see also [28, 33, 36]),

$$P^{(b)}(k, \eta) = 6P_{L0}(k) \int d\mathbf{k}' P_{L0}(k') F_3^s(\mathbf{k}', -\mathbf{k}', \mathbf{k}; \eta), \quad (59)$$

$$P^{(c)}(k, \eta) = 2 \int d\mathbf{k}' P_{L0}(k') P_{L0}(|\mathbf{k} - \mathbf{k}'|) F_2^s(\mathbf{k}', \mathbf{k} - \mathbf{k}'; \eta)^2. \quad (60)$$

B. Path-integral formulation

1. General formulation

The standard perturbative approach recalled in Sect. IV A computes the density power spectrum, and more generally many-body correlation functions, by first deriving an explicit expression for the nonlinear field $\tilde{\psi}$ in terms of the initial field $\tilde{\psi}_L$, as in Eqs.(50) and (52)-(53), up to some order, and second taking the Gaussian average over the initial conditions, as in Eq.(55).

It is possible to work in the reverse order, by first taking the average over the initial conditions and second writing an expansion in terms of the many-body correlations. A well-known procedure in the context of plasma physics and the study of the Vlasov equation is to use the BBGKY hierarchy, which gives a recursion between successive correlation functions that may be truncated at some order [37]. A similar approach has also been used in [30] to study the formation of large-scale structures in the single-flow perturbative regime, as in Eqs.(21)-(22). As described in [28, 31, 35], an alternative approach, also used in field theory and statistical physics [38, 39], is based on a path-integral formulation. There, it is shown that the statistical properties of the nonlinear field $\tilde{\psi}$, which are fully defined by the equation of motion (28) and the Gaussian initial conditions (35), can be obtained from the generating functional

$$Z[\tilde{j}] = \langle e^{\tilde{j} \cdot \tilde{\psi}} \rangle = \int \mathcal{D}\tilde{\psi} \mathcal{D}\tilde{\lambda} e^{\tilde{j} \cdot \tilde{\psi} - S[\tilde{\psi}, \tilde{\lambda}]}, \quad (61)$$

where $\tilde{\lambda}(x)$ is a Lagrange multiplier and the action $S[\tilde{\psi}, \tilde{\lambda}]$ reads as

$$S[\tilde{\psi}, \tilde{\lambda}] = \tilde{\lambda} \cdot (\mathcal{O} \cdot \tilde{\psi} - K_s \cdot \tilde{\psi} \tilde{\psi}) - \frac{1}{2} \tilde{\lambda} \cdot \Delta_I \cdot \tilde{\lambda} \quad (62)$$

Here Δ_I is the two-point correlation of the initial conditions, taken at a time η_I . This matrix disappears in the final equations when we take the limit $\eta_I \rightarrow -\infty$. Whereas moments of the field $\tilde{\psi}$ generate the many-body correlations of the density and velocity fields, such as the density power spectrum $P(k)$, moments that involve the

auxiliary field $\tilde{\lambda}$ generate the response functions [31, 39]. In particular, we have

$$\langle \tilde{\lambda} \rangle = 0, \quad \langle \tilde{\lambda} \tilde{\lambda} \rangle = 0, \quad \langle \tilde{\psi}(x_1) \tilde{\lambda}(x_2) \rangle = R(x_1, x_2). \quad (63)$$

As explained in [28, 35], the standard perturbative results of Sect. IV A can be recovered from the generating functional (61). Indeed, one can see at once from Eq.(51) that the expansion (50) is also an expansion over powers of the vertex K_s , with $\tilde{\psi}^{(n)} \propto K_s^{n-1}$ and $F_n^s \propto K_s^{n-1}$. Therefore, the standard expansion in powers of $\tilde{\delta}_{L0}$ for $\tilde{\psi}$, which leads to the usual expansion in powers of P_{L0} for averaged quantities, such as the density power spectrum (56), is identical to an expansion in K_s . Then, this expansion can be directly obtained from Eq.(61) by expanding in the cubic part $\tilde{\lambda} \cdot K_s \cdot \tilde{\psi} \tilde{\psi}$ of the action (62). This gives an alternative expression of the expansion (55) in terms of Feynman's diagrams[77].

2. Direct steepest-descent expansion

One interest of the expression (61) is that it can also serve as the basis of other approximation schemes. Here we focus on the “direct steepest-descent” method described in [28, 35], which is compared with numerical simulations for the density power spectrum and bispectrum in [32, 40]. In this approach, instead of expanding the cubic part of the action to write Eq.(61) as a series of Gaussian integrals, one expands around a saddle-point (which depends on \tilde{j}) as in a semi-classical or “large-N” expansion [41, 42]. This yields the Schwinger-Dyson equations

$$\mathcal{O} \cdot C = \Sigma \cdot C + \Pi \cdot R^T, \quad (64)$$

$$\mathcal{O} \cdot R = \delta_D + \Sigma \cdot R, \quad (65)$$

for the nonlinear two-point correlation C and response R , where Σ and Π are “self-energy” terms (there are two “correlations”, C and R , and two “self-energies”, Σ and Π , because there are two fields, the physical field ψ and the auxiliary field λ).

These equations are exact and define Σ and Π . The “direct steepest-descent” or “large-N” expansion scheme corresponds to writing the self-energy terms Σ and Π as series in powers of the linear correlation C_L and response R_L . Then, the order of the approximation is set by the order of the truncation chosen for these expansions of Σ and Π . Because the truncation is made on Σ and Π , rather than on C and R , this automatically yields a partial resummation of higher-order terms (e.g., formally R would be given by the highly nonlinear expression $(\mathcal{O} - \Sigma)^{-1}$ whose expansion in P_{L0} contains terms of all orders as soon as Σ contains at least one power of P_{L0}). As described in [28, 35, 41], the result obtained for the correlation C at a given order (e.g., at one-loop order as in this paper) agrees with the result obtained by the standard perturbative expansion at the same order, and

only differs by additional higher-order terms (which are only partially resummed).

Then, this “direct steepest-descent” scheme gives at the one-loop order

$$\begin{aligned} \Sigma^{\text{1loop}}(x, y) &= 4K_s(x; x_1, x_2)K_s(z; y, z_2)R_L(x_1, z) \\ &\times C_L(x_2, z_2), \end{aligned} \quad (66)$$

$$\begin{aligned} \Pi^{\text{1loop}}(x, y) &= 2K_s(x; x_1, x_2)K_s(y; y_1, y_2)C_L(x_1, y_1) \\ &\times C_L(x_2, y_2). \end{aligned} \quad (67)$$

This corresponds to a one-loop diagram [28, 32, 35] and at this order $\Sigma \propto P_{L0}$ while $\Pi \propto P_{L0}^2$. Substituting into Eqs.(64)-(65) gives the nonlinear correlation complete up to order P_{L0}^2 , as in (56), with the addition of a partial resummation of higher-order terms. Equation (64) can be solved as

$$C(x_1, x_2) = R \times C_L(\eta_I) \times R^T + R \cdot \Pi \cdot R^T, \quad (68)$$

where the first product does not contain any integration over time, and we take $\eta_I \rightarrow -\infty$. Thus, to compute the density power spectrum up to one-loop order within the direct steepest-descent resummation, we first compute the linear correlation C_L and R_L , given by Eqs.(44) and (49). This provides the self-energies Σ and Π from Eqs.(66) and (67). Next, we compute R by solving the integro-differential equation (65) and C from the explicit expression (68).

The formalism used for the Λ CDM cosmology still applies to our modelization of modified gravity. However, the numerical computation is somewhat heavier. Indeed, as described in [28, 32], in the Λ CDM case, the approximation $\Omega_m/f^2 \simeq 1$ allows us to explicitly factor the time-dependence of the linear correlation and response functions, and of the self-energies. Here this is no longer possible, because of the arbitrary function $\epsilon(k, \eta)$ in the linear operator (29). This makes the numerical implementation slightly more complex, as we can no longer use these factorizations to simplify the algorithms and we must keep track of the complex dependence on time and wavenumber of all linear modes and two-point functions. However, the method remains exactly the same, as described above, and it is still possible to devise efficient and reasonably fast numerical codes.

3. Recovering the standard one-loop results

Since we compute the self-energies Σ and Π for the one-loop steepest-descent scheme, we can also use them to recover the standard perturbative expansion instead of using the standard procedure recalled in Sect. IV A. Indeed, the solution of Eq.(65) can be written as the expansion over powers of Σ ,

$$R = R_L + R_L \cdot \Sigma \cdot R \quad (69)$$

$$= R_L + R_L \cdot \Sigma \cdot R_L + R_L \cdot \Sigma \cdot R_L \cdot \Sigma \cdot R_L + \dots \quad (70)$$

Therefore, up to order P_{L0} we can write

$$R = R^{(0)} + R^{(1)}, \quad (71)$$

with

$$R^{(0)} = R_L, \quad R^{(1)} = R_L \cdot \Sigma^{\text{1loop}} \cdot R_L. \quad (72)$$

Then, from (68) the two-point correlation reads up to order P_{L0}^2 as

$$C = C^{(1)} + C^{(2)}, \quad (73)$$

with

$$C^{(1)} = R_L \times C_L(\eta_I) \times R_L^T = C_L, \quad (74)$$

and

$$C^{(2)} = R^{(1)} \times C_L(\eta_I) \times R_L^T + R_L \times C_L(\eta_I) \times R^{(1)T} + R_L \cdot \Pi^{\text{1loop}} \cdot R_L^T. \quad (75)$$

This expression is equivalent to Eqs.(56)-(60) for the density power spectrum [35]. Therefore, since we have already computed Σ and Π we can compute the standard one-loop power spectrum through Eqs.(74)-(75), instead of using Eqs.(59)-(60). This avoids explicitly computing the n -point kernels F_n^s of the standard expansion (52).

A similar procedure, based on the closure approximation [29], which is equivalent (at one-loop order) to the “2PI” effective action method of [28], was used in [43] to obtain the standard perturbative predictions for several modified gravity models. However, while [43] included quadratic and cubic nonlinearities in the scalar field, associated with the onset of the chameleon mechanism, in this paper we only consider modifications to the Poisson equation at the linear level. On the other hand, within our simpler formulation of modified gravity we go beyond the standard perturbative approach by computing the “steepest-descent” resummation presented in the previous section.

4. Alternative resummations

Finally, the path-integral (61) can also lead to alternative resummation schemes, such as the “1PI” and “2PI” effective action methods described in [41]. The 2PI effective action still leads to the Schwinger-Dyson equations (64)-(65) but the self-energy terms are given in terms of the nonlinear two-point functions C and R , instead of the expansion over C_L and R_L used in the direct steepest-descent scheme. At one-loop order, this amounts to replacing C_L and R_L by C and R in Eqs.(66)-(67). However, already for the Λ CDM case this makes the computation more complex since Eqs.(64)-(65) become coupled nonlinear equations over C and R [28, 29]. Then, one needs to solve for the four quantities C , R , Σ , and Π by simultaneously moving forward with time. This numerical computation was performed in [28] and it appeared

that it did not provide a significant improvement over the simpler direct steepest-descent scheme (although a more precise comparison with numerical simulations may remain of interest). Therefore, we do not investigate this scheme further.

The direct steepest-descent method of Sect. IV B 2 is not necessarily the most accurate resummation scheme. In particular, it yields a response function that does not decay at high k or late times, but shows increasingly fast oscillations with an amplitude that follows the linear response function. This is not realistic, since one expects a Gaussian-like decay for Eulerian response functions, as can be seen from theoretical arguments and numerical simulations [27, 31, 44–46]. However, the fast oscillations still provide an effective damping in a weak sense (that is when the response function is integrated over). Alternative resummation schemes have also been studied in the literature, such as the “renormalized perturbation theory” [27, 44] and several related approaches [47–49], which rely on a response function that interpolates between its low- k standard perturbative expression and a resummed high- k limit, methods based on path-integral formulations [50], on closures of the hierarchies satisfied by the correlation functions [29, 30], or on Lagrangian-space formulations [51].

The reason why we consider the direct steepest-descent method here is that it provides a simple and efficient method, which has already been shown to be reasonably accurate for Λ CDM cosmology [32, 40]. An advantage with respect to some alternative approaches, which can show similar levels of accuracy, is that it is fully systematic and contains no free parameter or interpolation procedure. Therefore, the generalization from the Λ CDM cosmology to modified-gravity scenarios is straightforward, as described in Sect. IV B 2, and we can expect a similar accuracy.

C. Bispectrum

Because the gravitational dynamics is nonlinear, the density field becomes increasingly non-Gaussian in the course of time. The most popular measure of these non-Gaussianities, which can be used to break degeneracies between cosmological parameters or to constrain primordial non-Gaussianities, is the three-point correlation function [53]. In Fourier space this is the so-called bispectrum,

$$\langle \tilde{\delta}(\mathbf{k}_1) \tilde{\delta}(\mathbf{k}_2) \tilde{\delta}(\mathbf{k}_3) \rangle = \delta_D(\mathbf{k}_1 + \mathbf{k}_2 + \mathbf{k}_3) B(k_1, k_2, k_3). \quad (76)$$

This can be computed by the standard perturbative approach [33]. Substituting the expansion (52) yields the standard tree-order result

$$B^{\text{tree}}(k_1, k_2, k_3) = 2F_2^s(\mathbf{k}_2, \mathbf{k}_3; \eta) P_{L0}(k_2) P_{L0}(k_3) + 2 \text{ cyc.} \quad (77)$$

where “2 cyc.” stands for two terms obtained by circular permutations over $\{k_1, k_2, k_3\}$.

Within the path-integral formalism of Sect. IV B 1, expanding Eq.(61) in powers of K_s , that is, in the cubic part of the action S , yields for the three-point correlation at tree-order [35]

$$C_3^{\text{tree}} = R_L \cdot K_s \cdot C_L C_L + 5 \text{ perm.} \quad (78)$$

This gives for the equal-time density bispectrum:

$$\begin{aligned} B^{\text{tree}}(k_1, k_2, k_3; \eta) &= 2 \int_{-\infty}^{\eta} d\eta' \sum_{i'_1, i'_2, i'_3} R_{L;1,i'_1}(k_1; \eta, \eta') \\ &\times C_{L;1,i'_2}(k_2; \eta, \eta') C_{L;1,i'_3}(k_3; \eta, \eta') \\ &\times \gamma_{i'_1, i'_2, i'_3}^s(\mathbf{k}_2, \mathbf{k}_3) + 2 \text{ cyc.} \end{aligned} \quad (79)$$

which is again equivalent to Eq.(77). In practice, instead of Eq.(77) we use Eq.(79) to compute the standard tree-order bispectrum. The effects of the modified-gravity function $\epsilon(k, a)$ are included through the linear correlation and response C_L and R_L , which depend on the modified linear modes $D_+(k, a)$ and $D_-(k, a)$ as described in Sect. III. As in Sect. IV B 3, this allows us to obtain the “standard” perturbative predictions without computing the kernels F_n^s of Eq.(52).

At one-loop order the expressions involve more terms. They can be found in [35] (for the Λ CDM cosmology) for the standard approach as in (77), the equivalent path-integral formulation as in (79), and the direct steepest-descent method used in Sect. IV B 2 for the power spectrum. Contrary to the power spectrum, a detailed comparison with numerical simulations [40] shows that at one-loop order the steepest-descent resummation for the bispectrum is not more accurate than the standard result. Therefore, we do not investigate this resummation for the bispectrum here.

Because the linear modes depend on wavenumber, computing the one-loop order terms is significantly more difficult than in the Λ CDM case, even within standard perturbation theory. Using the scalings $B^{\text{tree}} \propto D_+^4 P_{L0}^2$ and $B^{\text{1loop}} \propto D_+^6 P_{L0}^3$, we consider the following approximation:

$$B^{\text{1loop}} \simeq \left(\frac{B^{\text{tree}}}{B_{\Lambda\text{CDM}}^{\text{tree}}} \right)^{3/2} B_{\Lambda\text{CDM}}^{\text{1loop}}. \quad (80)$$

Thus, we simply rescale the one-loop correction obtained in the Λ CDM scenario by the prefactor $(B^{\text{tree}}/B_{\Lambda\text{CDM}}^{\text{tree}})^{3/2}$. This would be exact if the ratio of the linear modes were constant. We choose this prefactor, rather than $(D_+(k)/D_{+,\Lambda\text{CDM}}(k))^6$, because it includes an integration over the past history and over the appropriate range of wavenumbers of the linear modes. This should be sufficient for our purpose, which is simply to estimate the magnitude of these one-loop corrections.

D. Numerical results

1. Set up

For our numerical computations, we adopt in this paper a flat Λ CDM reference model with cosmological parameters $(\Omega_m, \Omega_b, h, \sigma_8, n_s) = (0.279, 0.046035, 0.701, 0.817, 0.96)$, which is consistent with WMAP 5-year observations [54]. We use a publicly available code, CAMB [55], to compute the linear power spectrum including baryon acoustic oscillations. This is the same cosmology as used in [32, 40], which allows a clear comparison with their Λ CDM results. Then, the four models that we consider in this paper, defined by the parameters $(n, m_0) = (1, 0.1), (1, 1), (0, 0.1)$, and $(0, 1)$, as described in Sect. II B, are defined by the same initial conditions as this reference Λ CDM model. This means that they all coincide at early times and on large scales, because $\epsilon(k, a) \rightarrow 0$ for $a \rightarrow 0$ or $k \rightarrow 0$, but their linear variance σ_8 today on scale $8h^{-1}\text{Mpc}$ slightly differs.

For later use, let us note $\delta_{L(\Lambda)}(\mathbf{x}, \eta)$ the linear density field within the reference Λ CDM cosmology,

$$\tilde{\delta}_{L(\Lambda)}(\mathbf{k}, \eta) = D_{+(\Lambda)}(\eta) \tilde{\delta}_{L0}(\mathbf{k}), \quad (81)$$

where $D_{+(\Lambda)}$ is the Λ CDM linear growing mode, which does not depend on wavenumber. Then, the actual linear density field can be written in terms of this reference Λ CDM linear field as

$$\tilde{\delta}_L(\mathbf{k}, \eta) = \frac{D_+(k, \eta)}{D_{+(\Lambda)}(\eta)} \tilde{\delta}_{L(\Lambda)}(\mathbf{k}, \eta). \quad (82)$$

This is merely a re-writing of the initial conditions, which we choose to express at any time η through the reference Λ CDM growing mode.

2. Power spectrum

We show our results for the matter density power spectrum $P(k)$ on BAO (baryon acoustic oscillations [56]) scales in Fig. 6. To clearly distinguish the different curves and the baryon acoustic oscillations we normalize $P(k)$ by a smooth Λ CDM linear power spectrum $P_{Ls}(k)$ without baryon oscillations, from [52]. Our nonlinear prediction includes both the perturbative “two-halo” part $P_{2H}(k)$, based on the steepest-descent resummation (68), and the nonperturbative “one-halo” part $P_{1H}(k)$, as described in Sect. VIII and Eq.(124) below. However, on these scales the power spectrum is dominated by the perturbative contributions and the full nonlinear result is very close to the resummed perturbative part (68).

As explained above, all our results converge at low k to the same reference Λ CDM power, $P_{(\Lambda)}(k)$, because of our common choice of initial conditions. Moreover, on the scales shown in Fig. 6, this Λ CDM power spectrum cannot be distinguished from the $(n = 0, m_0 = 1)$

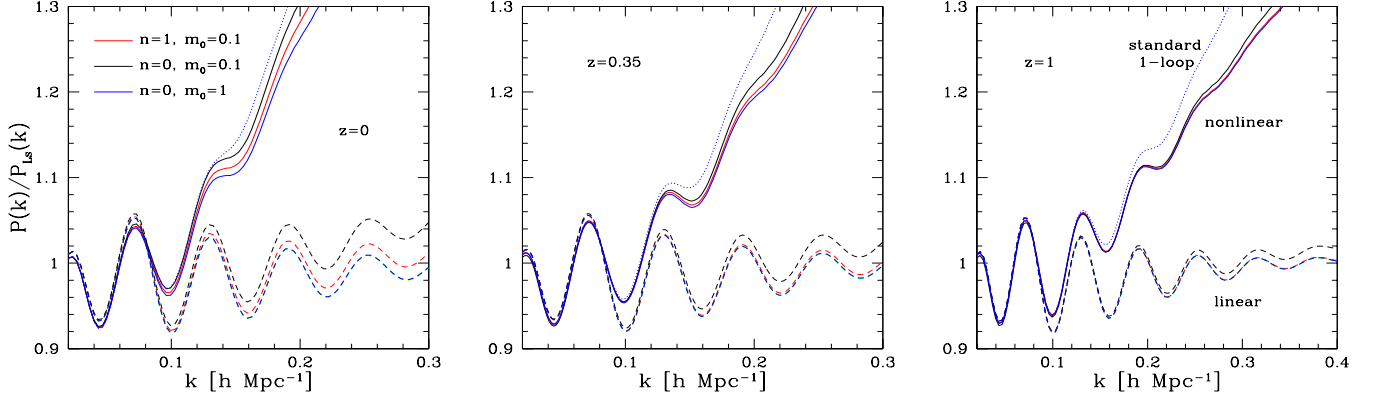


FIG. 6: Ratio of the power spectrum $P(k)$ to a smooth Λ CDM linear power spectrum $P_{Ls}(k)$ without baryonic oscillations, from [52]. We show our results for three models with $(n, m_0) = (1, 0.1)$ (middle red lines), $(0, 0.1)$ (upper black lines), and $(0, 1)$ (lower blue lines). In each case, we plot both the linear power (dashed line) and our nonlinear result (solid line) from Eq.(124), which is based on Eq.(68). For comparison, we also plot the standard 1-loop result from Eq.(73) for the case $(0, 1)$ (upper blue dotted line).

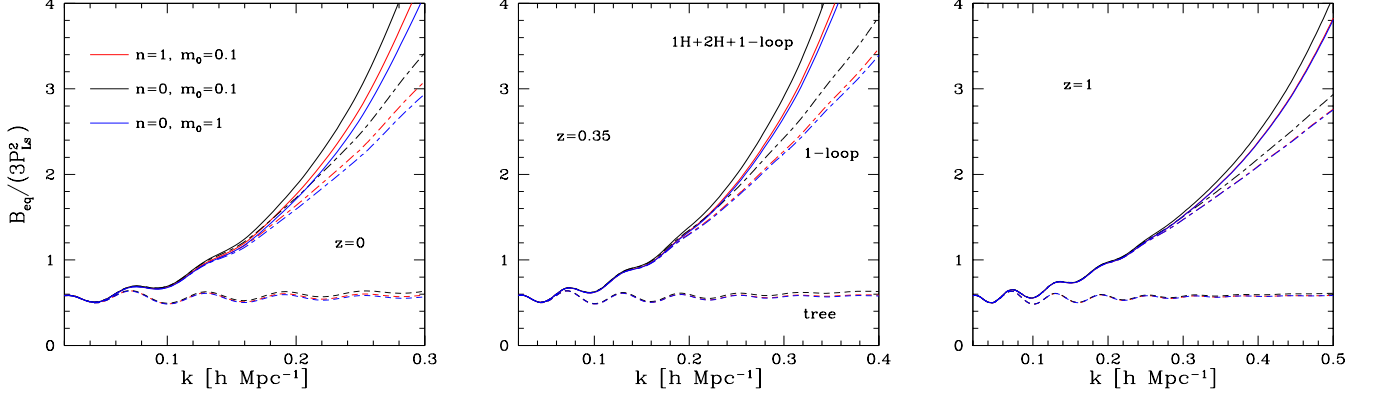


FIG. 7: Ratio of the equilateral bispectrum, $B_{eq}(k) = B(k, k, k)$, to the product $3P_{Ls}(k)^2$, where $P_{Ls}(k)$ is a smooth Λ CDM linear power spectrum without baryonic oscillations, from [52]. As in Fig. 6, we show our results for three models with $(n, m_0) = (1, 0.1)$ (middle red lines), $(0, 0.1)$ (upper black lines), and $(0, 1)$ (lower blue lines). In each case, we plot the tree-level bispectrum (dashed line) from Eq.(79), the 1-loop bispectrum (dash-dotted line) from Eq.(80), and our nonlinear result (solid line) from Eq.(128).

result, where the effects of modified gravity are the weakest amongst the models that we consider here. As in the Λ CDM cosmology, the nonlinear evolution amplifies the power spectrum but erases most of the oscillations. The difference between the various modified gravity models and General Relativity is rather small and it is not amplified by the nonlinear evolution. We clearly see that to probe these deviations it is necessary to go beyond linear theory and to include at least one-loop corrections. Moreover, the comparison with the upper dotted curve, which shows the standard one-loop result for the case $(n = 0, m_0 = 1)$ (which cannot be distinguished from GR), shows that these modified-gravity effects are at the order of or smaller than the accuracy of the standard one-loop prediction. This means that to probe modified

gravity on these scales it is necessary to use more accurate analytical formalisms, such as the resummation scheme described in Sect. IV B 2 and used in this paper, or to include higher-order corrections within the standard perturbative approach (but this latter option may not be very efficient because the standard perturbative expansion does not converge very well). This provides another motivation for the development of efficient perturbative schemes, which re-sum high-order contributions.

3. Bispectrum

We show our results for the matter density bispectrum on BAO scales in Fig. 7. Here we only consider equi-

lateral configurations, $B_{\text{eq}}(k) = B(k, k, k)$, and we normalize the bispectrum by $3P_{Ls}(k)^2$. Because $P_{Ls}(k)$ is not the actual power spectrum but a smooth Λ CDM linear power spectrum without baryon acoustic oscillations, this ratio is not identical to the usual “reduced bispectrum” $Q_{\text{eq}} = B_{\text{eq}}/(3P^2)$. However, this allows us to clearly distinguish the baryon acoustic oscillations of the tree-level bispectrum (77)-(79). Again, on these scales the Λ CDM bispectrum cannot be distinguished from the ($n = 0, m_0 = 1$) result.

As for the power spectrum shown in Fig. 6, the nonlinear evolution amplifies the bispectrum but erases most of the oscillations. The difference between the various models and GR is again rather small and it is necessary to go beyond the tree-level prediction. Unfortunately, the comparison between our approximate one-loop prediction and our full nonlinear model, which includes the non-perturbative “two-halo” and “one-halo” contributions as described in Sect. VIII below, suggests that one-loop terms are not sufficient to obtain reliable measures of such modified-gravity effects and that nonperturbative contributions cannot be neglected. Since the theoretical accuracy of such nonperturbative terms is lower than the one of perturbative terms (which can be computed in a systematic and rigorous fashion), this means that the bispectrum is not a very efficient probe of these modified-gravity models (unless one can run dedicated N-body simulations for each modified-gravity scenario). Thus, the power spectrum studied in Sect. IV D 2 should provide a better tool, as the accuracy of its theoretical predictions is better controlled.

V. SPHERICAL COLLAPSE

A. General case

To go beyond low-order perturbation theory, the main analytical tool that can provide exact nonlinear results is the study of the spherical collapse. This allows an explicit computation of the nonlinear dynamics (restricted to spherical symmetry) that can also serve as a basis to evaluate several quantities of cosmological interest, such as the halo mass functions and the probability distributions of the density contrast. We describe in this section the equations that govern the spherical dynamics and give a simple approximation for typical fluctuations.

Following the usual approach for Λ CDM or quintessence cosmologies [57, 58], the physical radius $r(t)$, which contains a constant mass M until shell-crossing, evolves as

$$\ddot{r} = -\frac{\partial \Psi}{\partial r} = -\frac{1}{a} \frac{\partial \Psi}{\partial x}, \quad \text{with} \quad \Psi = \Phi_N + \Psi_\epsilon, \quad (83)$$

where Ψ is the total potential seen by massive particles. Here we note with a dot derivatives with respect to time t , physical coordinates by \mathbf{r} and comoving coordinates by \mathbf{x} . Within our framework, defined by Eqs.(21)-(22), the

potential Ψ contains two parts, the usual Newtonian potential $\Psi_N = \Phi_N$, associated with General Relativity, and the effective component Ψ_ϵ , associated with the modification of gravity.

In physical coordinates, we have

$$\nabla_{\mathbf{r}}^2 \Phi_N = 4\pi\mathcal{G} \left(\rho_{\text{m}}^{(\text{phys.})} + (1 + 3w)\bar{\rho}_{\text{de}}^{(\text{phys.})} \right), \quad (84)$$

where we note with a superscript “(phys.)” densities in physical coordinates and we again assumed an uniform dark energy component. Using Gauss’ theorem, this yields the usual part $(\ddot{r})_N$ of the acceleration of the shell at radius r [57, 58],

$$(\ddot{r})_N = -\frac{4\pi\mathcal{G}}{3} r \left[\rho_{\text{m}}^{(\text{phys.})}(< r) + (1 + 3w)\bar{\rho}_{\text{de}}^{(\text{phys.})} \right], \quad (85)$$

where $\rho_{\text{m}}^{(\text{phys.})}(< r)$ is the mean physical density within radius r ,

$$\rho_{\text{m}}^{(\text{phys.})}(< r) = \frac{3M}{4\pi r^3}. \quad (86)$$

In comoving coordinates (with the background Hubble flow), the effective component Ψ_ϵ only depends on the matter density fluctuations, $\delta\rho_{\text{m}} = \rho_{\text{m}} - \bar{\rho}_{\text{m}}$, through

$$\tilde{\Psi}_\epsilon = \epsilon(k, t) \delta\Phi_N \quad \text{with} \quad \nabla^2(\delta\Phi_N) = 4\pi\mathcal{G}\delta\rho_{\text{m}}/a, \quad (87)$$

whence

$$\tilde{\Psi}_\epsilon(\mathbf{k}, t) = -\frac{4\pi\mathcal{G}\bar{\rho}_{\text{m}}}{ak^2} \epsilon(k, t) \tilde{\delta}(\mathbf{k}, t). \quad (88)$$

This is a linear approximation in the spherical collapse dynamics which is only valid as long as the screening effects of modified gravity are not taken into account. When the screening effects appear, the scalar force leading to the extra contribution in Newton’s equation is highly suppressed and the spherical over density collapses like in GR. These effects can be modeled out in the top-hat approximation like in [20] or using the exclusion set theory [21]. Taking into account these effects is left for future work.

Going back to configuration space, this yields the additional part $(\ddot{r})_\epsilon$ due to this “fifth force”,

$$(\ddot{r})_\epsilon = -\frac{4\pi\mathcal{G}}{3} r \bar{\rho}_{\text{m}}^{(\text{phys.})} \int_0^\infty dk 4\pi k^2 \epsilon(k) \tilde{\delta}(k) \tilde{W}(kx), \quad (89)$$

where the integral is written in terms of comoving quantities and $x = r/a$. Here we introduced the Fourier transform of the 3D top-hat of radius x and volume V ,

$$\tilde{W}(kx) = \int_V \frac{d\mathbf{x}'}{V} e^{i\mathbf{k}\cdot\mathbf{x}'} = 3 \frac{\sin(kx) - kx \cos(kx)}{(kx)^3}. \quad (90)$$

If ϵ does not depend on wavenumber we can check that Eq.(89) gives

$$(\ddot{r})_\epsilon = -\epsilon \frac{4\pi\mathcal{G}}{3} r \bar{\rho}_{\text{m}}^{(\text{phys.})} \delta(< x) \quad (91)$$

$$= -\epsilon \frac{4\pi\mathcal{G}}{3} r \left[\rho_{\text{m}}^{(\text{phys.})}(< r) - \bar{\rho}_{\text{m}}^{(\text{phys.})} \right]. \quad (92)$$

In agreement with Eq.(85), an uniform $\epsilon(t)$ gives rise to a fifth force that is proportional to the Newtonian gravitational force where we subtract the background part (associated with the mean density of the universe).

Collecting Eqs.(85) and (89) we obtain the equation of motion

$$\ddot{r} = -\frac{4\pi\mathcal{G}}{3}r \left[\rho_m^{(\text{phys.})}(<r) + (1+3w)\bar{\rho}_{\text{de}}^{(\text{phys.})} + \bar{\rho}_m^{(\text{phys.})} \int_0^\infty dk 4\pi k^2 \epsilon(k) \tilde{\delta}(k) \tilde{W}(kx) \right]. \quad (93)$$

As in [57, 58], it is convenient to introduce the normalized radius $y(t)$ defined as

$$y(t) = \frac{r(t)}{a(t)q} \quad \text{with} \quad q = \left(\frac{3M}{4\pi\bar{\rho}_m} \right)^{1/3}, \quad y(t=0) = 1. \quad (94)$$

Thus, q is the Lagrangian comoving coordinate of the shell $r(t)$, that is, the comoving radius that would enclose the same mass M in a uniform universe with the same cosmology. This also implies

$$\frac{\rho_m^{(\text{phys.})}(<r)}{\bar{\rho}_m^{(\text{phys.})}} = y^{-3}, \quad \delta_r \equiv \delta(<r) = y^{-3} - 1. \quad (95)$$

Choosing again $\eta = \ln a(t)$ as the time coordinate, as in the previous sections, Eq.(93) reads as

$$\frac{\partial^2 y}{\partial \eta^2} + \left(\frac{1}{2} - \frac{3}{2}w\Omega_{\text{de}} \right) \frac{\partial y}{\partial \eta} + \frac{\Omega_m}{2} (y^{-3} - 1) y = -\frac{\Omega_m}{2} y \int_0^\infty dk 4\pi k^2 \epsilon(k) \tilde{\delta}(k) \tilde{W}(kx). \quad (96)$$

The left hand side is the usual result in Λ CDM cosmology [57, 58] and the right hand side is the new term associated with the “fifth force”. If ϵ does not depend on wavenumber, the integral reduces to $\epsilon(a)\delta(<x) = \epsilon(y^{-3}-1)$, as in the usual third term of the left hand side. Then, the motion of each mass shell, described by $y(M, \eta)$ or $r(M, \eta)$, is independent of the other shells before shell crossing. If $\epsilon(k, a)$ depends on wavenumber, the integral does not reduce to a simple function of y at the same mass scale and it explicitly depends on the whole density profile, $\delta(x)$ or $\tilde{\delta}(k)$ in Fourier space, of the matter perturbation. Then, the dynamics of all mass shells are coupled at all times, even before shell crossing, and we must solve for the evolution of the full density profile with time, $y(M, \eta)$, as a function of M and η .

In previous works [22, 59], the spherical collapse dynamics was often approximated through an effective rescaling of Newton’s constant (this corresponds to a function $\epsilon(a)$ that does not depend on k). This allows one to recover the usual form of the equations of motion where all shells are decoupled before shell crossing. By varying this effective Newton constant [22], or making it a dynamical variable that depends on the environment [59], one may capture screening effects. Here we do not

include such screening effects but Eq.(96) takes into account the dependence of the dynamics on the density profile. This allows us to include the effects associated with the dependence on wavenumber of $\epsilon(k, a)$. As we will check in Fig. 8 below, this already yields a dependence on mass of the linear density threshold $\delta_c(M)$ associated with halo formation.

Thus, the modified-gravity term makes the equation of motion significantly more complex, because it is no longer local and it turns the usual ordinary differential equation into a partial integro-differential equation.

B. Approximation for typical profiles

Let us assume we are interested in the dynamics of a single mass shell M . Then, we wish to obtain from Eq.(96) a closed approximate equation for $y_M(\eta) \equiv y(M, \eta)$, which does not involve the other shells M' . The simplest method is to use an ansatz for the density profile $\delta(x, \eta)$, or $\tilde{\delta}(k, \eta)$, that is parameterized by $y_M(\eta)$. This will simplify numerical computations because it will transform Eq.(96) into a single ordinary differential equation. Then, let us recall that the mean conditional profile of the linear density contrast $\delta_L(\mathbf{x})$, under the constraint that the mean density contrast within a comoving radius R is equal to δ_{LR} , reads as [60]

$$\delta_L(\mathbf{x}) = \frac{\delta_{LR}}{\sigma_R^2} \int_V \frac{d\mathbf{x}'}{V} C_{\delta_L \delta_L}(\mathbf{x}, \mathbf{x}'), \quad (97)$$

where $C_{\delta_L \delta_L}$ is the matter density linear correlation,

$$C_{\delta_L \delta_L}(\mathbf{x}_1, \mathbf{x}_2) = \langle \delta_L(\mathbf{x}_1) \delta_L(\mathbf{x}_2) \rangle = \int_0^\infty dk 4\pi k^2 P_L(k) \frac{\sin(k|\mathbf{x}_2 - \mathbf{x}_1|)}{k|\mathbf{x}_2 - \mathbf{x}_1|}, \quad (98)$$

and σ_R^2 is the variance of the linear density contrast at scale R ,

$$\sigma_R^2 = \langle \delta_{LR}^2 \rangle = \int_0^\infty dk 4\pi k^2 P_L(k) \tilde{W}(kR)^2. \quad (99)$$

This only relies on the assumption that the linear density field is Gaussian. Then, we consider the approximation where the density profile used in Eq.(96) is set to

$$\delta(\mathbf{x}) = \frac{\delta_{x_M}}{\sigma_{x_M}^2} \int_{V_M} \frac{d\mathbf{x}'}{V_M} C_{\delta_L \delta_L}(\mathbf{x}, \mathbf{x}'), \quad (100)$$

which reads in Fourier space as

$$\tilde{\delta}(k) = \frac{y_M^{-3} - 1}{\sigma_{x_M}^2} P_L(k) \tilde{W}(kx_M), \quad (101)$$

where we used $\delta_{x_M} = y_M^{-3} - 1$. Here $x_M(\eta) = r_M(\eta)/a(\eta) = y_M(\eta)q_M$ is the comoving radius of the

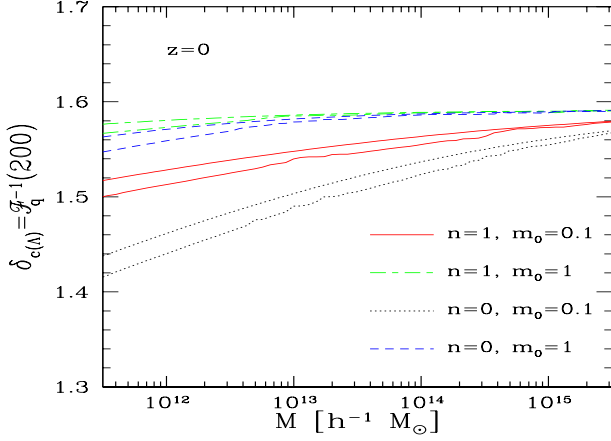


FIG. 8: Reference linear density contrast $\delta_{c(\Lambda)} = \mathcal{F}_q^{-1}(200)$ associated with a nonlinear density threshold of 200 at redshift $z=0$. We show our results as a function of the halo mass M for four (n, m_0) models, for typical initial profiles of the form (104). In each case, the upper curve is the approximate result from Eq.(102) and the lower curve the exact result from Eq.(96).

shell M and it follows its spherical dynamics. Substituting the ansatz (101) into Eq.(96) gives the equation of motion

$$\begin{aligned} \frac{d^2 y_M}{d\eta^2} + \left(\frac{1}{2} - \frac{3}{2} w \Omega_{de} \right) \frac{dy_M}{d\eta} + \frac{\Omega_m}{2} (y_M^{-3} - 1) y_M \\ \times \left(1 + \frac{1}{\sigma_{x_M}^2} \int_0^\infty dk 4\pi k^2 \epsilon(k) P_L(k) \tilde{W}(k x_M)^2 \right) = 0. \end{aligned} \quad (102)$$

The equation (102) is exact if ϵ does not depend on wavenumber, in which case the parenthesis is equal to $(1 + \epsilon(\eta))$ and we recover the behaviour of Eq.(92). It is also valid at order one over δ_L and ϵ when the initial perturbation has the linear profile (97) at early time. Thus, it agrees with the typical profile (97), under the constraint δ_{Lx_M} at mass shell M , in the linear regime, at zeroth order over ϵ . It is no longer exact at higher orders over δ_L because the nonlinear dynamics changes the shape of the density profile in a complex fashion. It is not valid at order ϵ , even in the linear regime, because the mean profile (97) is not a solution of the linear dynamics, as the linear growing mode $D_+(k, a)$ depends on wavenumber. In our case, where $\epsilon \ll 1$, this is a negligible effect and we would actually obtain similar results by using in Eqs.(100) and (101) the reference Λ CDM linear correlation $C_{\delta_L \delta_L}(\Lambda)$ and power $P_L(\Lambda)$.

C. Spherical-collapse mapping

In the linear regime we can check that Eq.(96) agrees with Eq.(34) for the linear growing mode. Indeed, using

$y_L = 1 - \delta_{Lq}/3$, $\delta_{Lq} = \int_V d\mathbf{x} \delta_L(\mathbf{x})/V$, and $x = q$ at lowest order, Eq.(96) becomes at linear order:

$$\int_V \frac{d\mathbf{x}}{V} \int d\mathbf{k} e^{i\mathbf{k} \cdot \mathbf{x}} \left\{ \frac{\partial^2 \tilde{\delta}_L}{\partial \eta^2}(\mathbf{k}) + \left(\frac{1}{2} - \frac{3}{2} w \Omega_{de} \right) \frac{\partial \tilde{\delta}_L}{\partial \eta}(\mathbf{k}) - \frac{3\Omega_m}{2} (1 + \epsilon(k)) \tilde{\delta}_L(\mathbf{k}) \right\} = 0. \quad (103)$$

This agrees with Eq.(34) and we recover the linear solution $\tilde{\delta}_L(\mathbf{k}, \eta) = D_+(k, \eta) \tilde{\delta}_{L0}(\mathbf{k})$.

At linear order, the ansatz (101) reads in Fourier-space as $\tilde{\delta}_L(\mathbf{k}) = (\delta_{Lq_M}/\sigma_{q_M}^2) P_L(k) \tilde{W}(k q_M)$. Substituting into Eq.(103) remains exact if the profile of the perturbation is given by Eq.(100) (or for the shell M , whatever the initial profile, if ϵ does not depend on wavenumber).

We now consider the spherical dynamics of typical initial perturbations, of the form (97) at early times, which we write as

$$\delta_{Lq'}(\Lambda) = \delta_{Lq(\Lambda)} \frac{\sigma_{q, q'(\Lambda)}^2}{\sigma_{q(\Lambda)}^2}, \quad (104)$$

for the mean initial density contrast within arbitrary radius q' . Here, as explained in Sect. IVD 1, we choose to write the initial conditions in terms of the reference Λ CDM linear field, which is simply an “update” at arbitrary time η of the initial field δ_{L0} given at a fixed time. This is more convenient than using the actual linear field δ_L , which depends on the modified-gravity growing mode $D_+(k, \eta)$ and mixes dependences on the initial conditions and on the modified gravity parameters. In this fashion, Eq.(104) describes the same initial condition for all our models. Here $\sigma_{q_1, q_2(\Lambda)}^2$ is the cross-correlation of the smoothed reference linear density contrast at scales q_1 and q_2 ,

$$\begin{aligned} \sigma_{q_1, q_2(\Lambda)}^2 &= \langle \delta_{Lq_1(\Lambda)} \delta_{Lq_2(\Lambda)} \rangle \\ &= \int_0^\infty dk 4\pi k^2 P_L(\Lambda)(k) \tilde{W}(k q_1) \tilde{W}(k q_2), \end{aligned} \quad (105)$$

and $\sigma_{q(\Lambda)}^2 = \sigma_{q, q(\Lambda)}^2$. For each mass scale q , with $M = (4\pi/3) \bar{\rho}_m q^3$, and initial amplitude $\delta_{Lq(\Lambda)}$, which define the initial condition (104), we can solve the spherical dynamics (96) or the approximate dynamics (102). For the “exact” dynamics (96) we consider for simplicity that inner shells that have already collapsed to the center of the halo remain at the center. (After shell crossing we should modify Eq.(96) to take into account the change with time of the mass enclosed within a given shell. However, we do not consider this effect because radial orbits suffer from a strong instability, which diverges at the time of collapse to the center [61], and after that time one should include transverse motions that lead to virialization.) As long as shell crossing is restricted to inner shells, within the mass scale M of interest, this is not a very serious problem because the dynamics is mostly sensitive to the total mass enclosed within a given radius (as in the usual Newtonian case or for ϵ that does not depend on wavenumber)

or to the local slope of the density profile (for the low- k behaviour $\epsilon(k) \propto k^2$).

At a given mass scale q and time η , this defines a mapping, $\delta_{Lq(\Lambda)} \mapsto \delta_x = \mathcal{F}_q(\delta_{Lq(\Lambda)})$, from the reference linear density contrast $\delta_{Lq(\Lambda)}$ to the nonlinear density contrast δ_x . Here x is again the Eulerian comoving radius of the shell M , with $x = r/a = yq$ as in (94).

If ϵ does not depend on wavenumber, this mapping does not depend on the scale q nor on the shape of the initial profile. If ϵ depends on wavenumber, this mapping depends both on the mass scale q (whence the subscript q in \mathcal{F}_q) and on the initial shape of the profile (which is why we had to choose a specific case, such as the typical shape (104)). This implies that if we choose for instance a given nonlinear density threshold, such as 200, to define halos, the associated linear density contrast $\delta_{c(\Lambda)} = \mathcal{F}_q^{-1}(200)$ depends on the mass of the halo (through the scale q).

We show our results for this linear density threshold $\mathcal{F}_q^{-1}(200)$ at redshift $z = 0$ in Fig. 8. For each model we plot both the exact result from Eq.(96) and the approximate result from Eq.(102). We clearly see the mass dependence associated with the modification of gravity. For positive ϵ gravitational clustering is more efficient and a lower value of $\delta_{L(\Lambda)}$ is required to reach the nonlinear density contrast $\delta = 200$. Because we recover General Relativity on large scales ($\epsilon \rightarrow 0$ for $k \rightarrow 0$) all curves converge to the Λ CDM threshold at large mass and show increasingly large deviations from GR at smaller mass.

Similar trends were obtained in [59], using a simplified dynamics described by an effective Newton constant that depends on the “environment” density, which allowed them to include screening effects. Thus, because the latter are more important for large mass they obtained a mass-dependent threshold δ_c that decreases at small mass and converges to the GR value at large mass. We can see in Fig. 8 that even without such screening effects, a dependence on mass is already present because of the dependence on wavenumber of $\epsilon(k, a)$. Since both effects show similar trends, including them both would give a steeper dependence on mass than in Fig. 8. Nevertheless, it is interesting to also investigate both mechanisms separately, as their relative amplitude depends on the details of the modified-gravity model.

We can see that the approximation (102) somewhat underestimates the departure from the GR result. This can be understood from the fact that the dynamics steepens the density profile, which amplifies the right hand side in Eq.(96). Nevertheless, the approximation (102), which is much easier to compute, gives a reasonable estimate of the modified-gravity effect. Because inner shells have already collapsed when the shell at mass M reaches the nonlinear threshold $\delta_x = 200$, we should include virialization effects which smooth out the inner density profile. Therefore, the difference seen in Fig. 8 should actually be somewhat overestimated. Moreover, for smaller nonlinear density contrast δ_x the relative deviation decreases, because the ansatz (100) is exact at linear order (for our initial conditions). Thus, for practical estimates the ap-

proximation (102) should be sufficient, at least in a first step.

VI. DENSITY CONTRAST PROBABILITY IN THE QUASILINEAR REGIME

Following [62, 63], we can use the spherical collapse dynamics described in Sect. V to derive the probability distribution of the matter density contrast in the quasilinear regime.

To compute the probability distribution, $\mathcal{P}(\delta_x)$, of the nonlinear density contrast within a sphere of comoving radius x , it is convenient to introduce the cumulant generating function

$$e^{-\varphi(y)/\sigma_{x(\Lambda)}^2} \equiv \left\langle e^{-y\delta_x/\sigma_{x(\Lambda)}^2} \right\rangle \quad (106)$$

$$= \int_{-1}^{\infty} d\delta_x e^{-y\delta_x/\sigma_{x(\Lambda)}^2} \mathcal{P}(\delta_x). \quad (107)$$

This determines the distribution $\mathcal{P}(\delta_x)$ through the inverse Laplace transform

$$\mathcal{P}(\delta_x) = \int_{-i\infty}^{+i\infty} \frac{dy}{2\pi i \sigma_{x(\Lambda)}^2} e^{[y\delta_x - \varphi(y)]/\sigma_{x(\Lambda)}^2}. \quad (108)$$

In Eqs.(107)-(108) we rescaled the cumulant generating function by a factor $\sigma_{x(\Lambda)}^2$ so that it has a finite limit in the quasilinear regime, $\sigma_{x(\Lambda)} \rightarrow 0$, for the case of Gaussian initial fluctuations [33]. In particular, its expansion at $y = 0$ reads

$$\varphi(y) = - \sum_{n=2}^{\infty} \frac{(-y)^n}{n!} \frac{\langle \delta_x^n \rangle_c}{\sigma_{x(\Lambda)}^{2(n-1)}}. \quad (109)$$

The average (106) can be written as the path-integral

$$e^{-\varphi(y)/\sigma_{x(\Lambda)}^2} = (\det C_{\delta_L \delta_L(\Lambda)}^{-1})^{1/2} \int \mathcal{D}\delta_{L(\Lambda)} e^{-S[\delta_{L(\Lambda)}]/\sigma_{x(\Lambda)}^2}, \quad (110)$$

where $C_{\delta_L \delta_L(\Lambda)}^{-1}$ is the inverse matrix of the two-point correlation of the reference linear density field and the action S reads as

$$S[\delta_{L(\Lambda)}] = y\delta_x[\delta_{L(\Lambda)}] + \frac{\sigma_{x(\Lambda)}^2}{2} \delta_{L(\Lambda)} \cdot C_{\delta_L \delta_L(\Lambda)}^{-1} \cdot \delta_{L(\Lambda)} \quad (111)$$

Here $\delta_x[\delta_{L(\Lambda)}]$ is the nonlinear functional which assigns to the initial condition, defined by the reference linear density field $\delta_{L(\Lambda)}(\mathbf{x}')$, the nonlinear density contrast δ_x within the sphere of radius x .

As in Sect. VC, we choose to define the initial conditions through the reference Λ CDM linear field $\delta_{L(\Lambda)}$. We could also write all expressions above in terms of the actual linear field δ_L , its correlation $C_{\delta_L \delta_L}$, and the variance σ_x^2 . Here we prefer the formulation (110) because it clearly separates the initial conditions from the modified-gravity effects. Thus, in the action (111) all modified-gravity effects are enclosed in the functional $\delta_x[\delta_{L(\Lambda)}]$,

which describes the gravitational dynamics, whereas if we express the initial conditions in terms of the ϵ -dependent linear field δ_L these modified gravity effects would appear in all terms of the action. Of course, we adopt this formulation because we wish to compare with this Λ CDM reference several models that only show small deviations.

The action S does not depend on the normalization of the linear power spectrum since both $\sigma_{x(\Lambda)}^2$ and $C_{\delta_L \delta_L(\Lambda)}$ are proportional to $P_{L(\Lambda)}$. Then, in the quasilinear limit, $\sigma_{x(\Lambda)} \rightarrow 0$, the path integral (110) is dominated by the minimum of the action [62],

$$\sigma_{x(\Lambda)} \rightarrow 0: \quad \varphi(y) \rightarrow \min_{\delta_{L(\Lambda)}(\mathbf{x}')} S[\delta_{L(\Lambda)}]. \quad (112)$$

Using the spherical symmetry of the top-hat window W that defines the spherical average δ_x , one obtains a spherical saddle-point [62]. In General Relativity its linear radial profile is given by Eq.(104), where q is the Lagrangian radius that corresponds to the Eulerian radius x ,

$$q^3 = (1 + \delta_x)x^3. \quad (113)$$

Then, the amplitude $\delta_{Lq(\Lambda)}$ of the saddle-point (104), which also sets the scale q through Eq.(113), is given by the spherical-collapse mapping,

$$\delta_x = \mathcal{F}(\delta_{Lq(\Lambda)}). \quad (114)$$

This derivation agrees with the results that can be obtained from a perturbative computation of the cumulants $\langle \delta_x^n \rangle_c$ at leading order and a resummation of the series (109) [60]. It also extends these results to the case where the series (109) has a zero radius of convergence, which occurs when $\mathcal{P}(\delta_x)$ decreases more slowly than a simple exponential at large densities [62] [78].

A nice feature of this derivation is that it bypasses the computation of the cumulants $\langle \delta_x^n \rangle_c$ through the kernels F_n^s of Eq.(52), as all spherically-averaged quantities are given by the spherical-dynamics mapping $\mathcal{F}(\delta_{L(\Lambda)})$ (which includes terms at all orders by expanding over $\delta_{L(\Lambda)}$). However, the problem is more complex in our case because of the dependence of $\epsilon(k, a)$ on wavenumber. Indeed, this means that the nonlinear density contrast δ_x at radius x does not depend on the linear density contrast $\delta_{Lq(\Lambda)}$ at the Lagrangian radius q , associated with the same mass M only. Indeed, as discussed in Sect. V, the spherical dynamics (96) depends on the full shape of the initial perturbation. Taking into account this modification changes the profile $\delta_{L(\Lambda)}(\mathbf{x}')$ of the minimum of the action $S[\delta_{L(\Lambda)}]$ in Eq.(112), because the functional $\delta_x[\delta_{L(\Lambda)}(\mathbf{x}')] is no longer of the form $\delta_x = \mathcal{F}(\delta_{Lq(\Lambda)})$.$

To simplify the analysis we neglect this change of the profile of the saddle-point. This is actually valid to first order over ϵ . Indeed, let us write the action S as $S = S_0 + \hat{\epsilon}S_1$, where S_0 is the usual Λ CDM action (where $\epsilon = 0$), and S_1 is the modification due to a nonzero $\epsilon(k, a)$ kernel, where we factored out a normalization parameter $\hat{\epsilon}$ that scales as ϵ . Because of

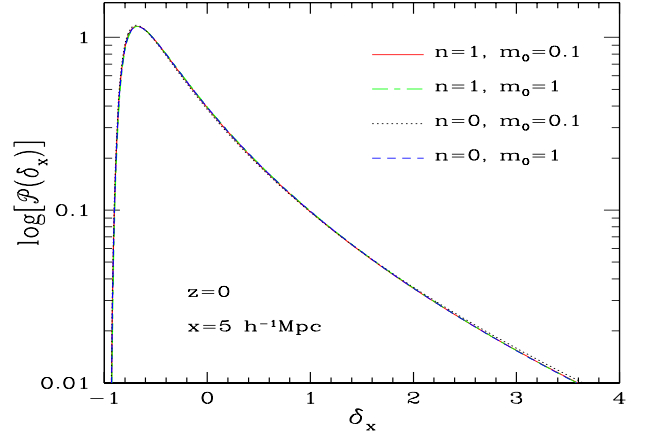


FIG. 9: Probability distribution of the matter density contrast within spherical cells of radius $5h^{-1}\text{Mpc}$ at $z=0$ (all curves almost fall on each other).

this new term $\hat{\epsilon}S_1$, the saddle-point $\delta_{L(\Lambda)}$ is changed to $\delta_{L(\Lambda)} = \delta_{L0(\Lambda)} + \hat{\epsilon}\delta_{L1(\Lambda)}$, where $\delta_{L0(\Lambda)}$ is the GR saddle-point (104). Then, the generating function is changed to $\varphi(y) \rightarrow S_0[\delta_{L0(\Lambda)} + \hat{\epsilon}\delta_{L1(\Lambda)}] + \hat{\epsilon}S_1[\delta_{L0(\Lambda)} + \hat{\epsilon}\delta_{L1(\Lambda)}]$. Because $\delta_{L0(\Lambda)}$ is a saddle-point of the action S_0 , we have $S_0[\delta_{L0(\Lambda)} + \hat{\epsilon}\delta_{L1(\Lambda)}] = S_0[\delta_{L0(\Lambda)}] + \mathcal{O}(\hat{\epsilon}^2)$, that is, $S_0[\delta_{L(\Lambda)}]$ is only modified by terms of order ϵ^2 . Because of the prefactor $\hat{\epsilon}$ we also have $\hat{\epsilon}S_1[\delta_{L0(\Lambda)} + \hat{\epsilon}\delta_{L1(\Lambda)}] = \hat{\epsilon}S_1[\delta_{L0(\Lambda)}] + \mathcal{O}(\hat{\epsilon}^2)$. Therefore, $S[\delta_{L(\Lambda)}] = S[\delta_{L0(\Lambda)}] + \mathcal{O}(\hat{\epsilon}^2)$ and we can neglect the change of the saddle-point up to first order over ϵ . In fact, we do better than this because we only neglect the change of the radial profile but we keep track of the dependence on ϵ of the amplitude $\delta_{Lq(\Lambda)}$ of the saddle-point.

On the other hand, if we use the approximation (102) instead of Eq.(96), the functional $\delta_x[\delta_{L(\Lambda)}(\mathbf{x}')] is again of the form $\delta_x = \mathcal{F}_q(\delta_{Lq(\Lambda)})$ and the saddle-point profile (104) becomes exact within this approximation.$

In both cases, whether we use the approximation (102) or the exact equation (96), the function \mathcal{F}_q now also depends on the scale q , in contrast to the usual Newtonian case.

Then, from this spherical-collapse mapping $\mathcal{F}_q(\delta_{Lq(\Lambda)})$, described in Sect. V C, we obtain the generating function $\varphi(y)$ as follows [62, 63]. Substituting the profile (104) into Eq.(111) and using Eq.(114) the minimum (112) reads as

$$\varphi(y) = \min_{\delta_{Lq(\Lambda)}} \left[y \mathcal{F}_q(\delta_{Lq(\Lambda)}) + \frac{1}{2} \frac{\sigma_{x(\Lambda)}^2}{\sigma_{q(\Lambda)}^2} \delta_{Lq(\Lambda)}^2 \right]. \quad (115)$$

Defining the function $\tau(\zeta)$ through the parametric system [62, 64],

$$\zeta = \delta_x = \mathcal{F}_q(\delta_{Lq(\Lambda)}) \quad \text{and} \quad \tau = -\delta_{Lq(\Lambda)} \frac{\sigma_{x(\Lambda)}}{\sigma_{q(\Lambda)}}, \quad (116)$$

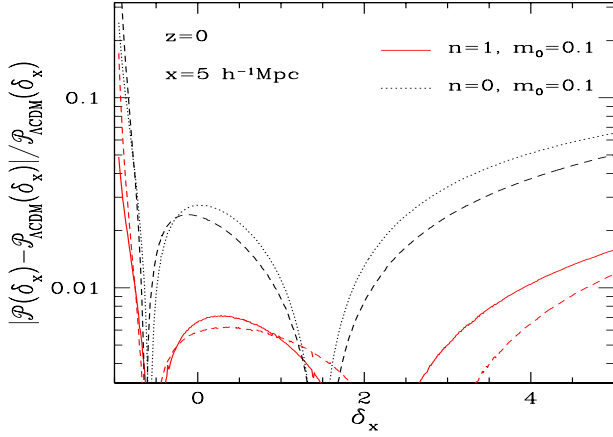


FIG. 10: Relative deviation from General Relativity of the probability distribution $\mathcal{P}(\delta_x)$, at redshift $z = 0$ for a radius $x = 5h^{-1}\text{Mpc}$. For each (n, m_0) model the deviation from GR is positive at low and high densities and negative around $\delta \sim 0$. The solid and dotted lines are the exact results from Eq.(96) for $(n, m_0) = (1, 0.1)$ and $(0, 0.1)$. The closest dashed line of the same color is the result from the approximation (102), for the same value of (n, m_0) .

the minimum (115) also writes as

$$\varphi(y) = \min_{\zeta} \left[y\zeta + \frac{\tau(\zeta)^2}{2} \right]. \quad (117)$$

This corresponds to the implicit equations (Legendre transform)

$$y = -\tau \frac{d\tau}{d\zeta} \quad \text{and} \quad \varphi = y\zeta + \frac{\tau^2}{2}. \quad (118)$$

Finally, this gives the probability distribution $\mathcal{P}(\delta_x)$ through Eq.(108). The probability distribution $\mathcal{P}(\delta_x)$ depends on the spherical-collapse dynamics and on the shape of the initial power spectrum $P_{L(\Lambda)}(k)$, through the ratio $\sigma_{x(\Lambda)}/\sigma_{q(\Lambda)}$ in the second Eq.(116). This second effect, sometimes called a “smoothing effect” [64], is due to the collapse (or expansion) of the mass shell M from the Lagrangian scale q to the Eulerian scale x . This mixes scales and implies that the distribution $\mathcal{P}(\delta_x)$ at scale x is sensitive to the initial power over all scales. In our modified-gravity case, a second dependence on the shape of the linear power spectrum appears through the mapping \mathcal{F}_q itself, because of the ϵ -dependent terms in Eqs.(96) and (102).

We show in Fig. 9 the probability distribution $\mathcal{P}(\delta_x)$ at redshift $z = 0$ and radius $x = 5h^{-1}\text{Mpc}$. Here we use the exact dynamics (96) but using the approximation (102) gives very close results that would not be distinguished in this figure. We recover the usual asymmetric shape due to nonlinear gravitational clustering, which builds an extended high-density tail and shifts the peak of the distribution towards low densities before a sharp low density

cutoff at $\delta_x \rightarrow -1^+$ (on small scales, most of the matter lies in overdensities but most of the volume lies in underdense regions).

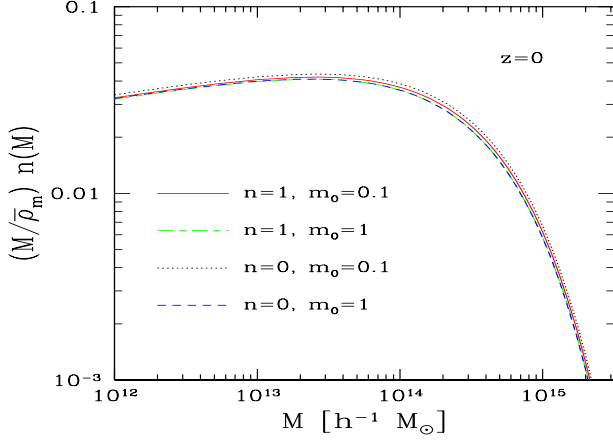
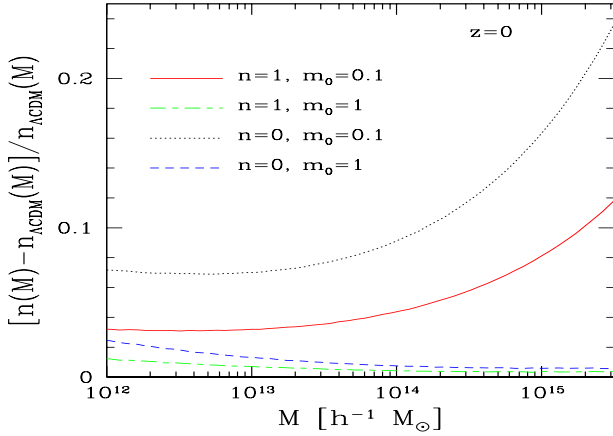
Since it is difficult to distinguish different curves on this figure we plot the relative deviation from GR in Fig. 10, for the two models where it is the largest. (The two other cases would fall below the range plotted in the figure for the most part.) We plot our results using either the exact equation (96) or the approximation (102). We can see that both curves are very close. Indeed, as explained in Sect. V C, for smaller density fluctuations the ansatz (100) becomes more accurate as it is exact to linear order and the profile has not had time to be strongly modified by the dynamics (moreover, the collapse is not very sensitive to the exact shape of the profile).

As we consider models with a positive value of ϵ , which leads to an effective amplification of gravity, it is easier to build large nonlinear density fluctuations. This was also apparent in Fig. 8 for the specific case of $\delta_x = 200$. For Gaussian initial conditions the tails of the probability distribution $\mathcal{P}(\delta_x)$ are of the form $\mathcal{P}(\delta_x) \sim e^{-\delta_{Lq(\Lambda)}^2/(2\sigma_{q(\Lambda)}^2)}$, where $\delta_{Lq(\Lambda)} = \mathcal{F}_q^{-1}(\delta_x)$, and the lower value of $|\delta_{Lq(\Lambda)}|$ that is needed to reach a given $|\delta_x|$ yields a slower decay of the rare-event tails. This is why we recover a positive deviation from GR (i.e., a higher probability \mathcal{P}) at both very low and very high densities in Fig. 10. Of course, since probability distributions are always normalized to unity this implies that the relative deviation shows a change of sign and that the probability distribution $\mathcal{P}(\delta_x)$ obtained in these models is smaller than the ΛCDM one for moderate densities. This explains the behaviours seen in Fig. 10.

These features are in qualitative agreement with the results obtained in numerical simulations of various modified gravity models [65, 66], which also find that an effective amplification of gravity generically leads to more numerous very low density and high density regions, while shifting the peak of the probability distribution towards lower densities.

The relative deviation from GR does not necessarily grow to unity at high densities (and may even decline). This is due to the fact that high densities at a given Eulerian radius x correspond to large masses, hence to large Lagrangian (i.e. initial) radius q . Then, because we recover General Relativity on large scales the linear threshold $\delta_{Lq(\Lambda)} = \mathcal{F}_q^{-1}(\delta_x)$ converges to the one obtained in the ΛCDM cosmology, as in Fig. 8. Therefore, depending on the rate of convergence towards General Relativity on large scales (as compared with the increasingly high sensitivity of the rare tail) the large-density tail may or may not converge back to the GR prediction. In modified gravity scenarios with a screening mechanism that implies convergence to GR in high-density environments, such as the chameleon mechanism, the high-density tail is expected to show a faster convergence back to the GR prediction.

These effects do not appear at very low densities, which correspond to increasingly small mass M and Lagrangian

FIG. 11: Halo mass function at redshift $z = 0$.FIG. 12: Relative deviation from Λ CDM of the halo mass function at redshift $z = 0$.

radius q , where the modifications from General Relativity do not vanish within our framework. In this limit, the relative deviation of $\mathcal{P}(\delta_x)$ from the Λ CDM reference can grow up to unity. However, this appears far in the low-density tail, which is characterized by a very sharp cutoff, and this may not be a very efficient tool to probe modified-gravity effects.

VII. HALO MASS FUNCTION

The computation of the probability distribution $\mathcal{P}(\delta_x)$ was described in the previous section for the quasilinear regime, $\sigma_{x(\Lambda)} \rightarrow 0$. However, this result is more general and actually applies to rare events, where the path integral (110) is peaked around the minimum of the action S . In the quasilinear limit any finite nonzero density contrast δ_x becomes a rare event, which is why Eq.(117) determines the full probability distribution in this regime.

For arbitrary values of σ_x , Eq.(117) applies to rare events, that is, to the tails of the probability distribution $\mathcal{P}(\delta_x)$ [61] (this again allows one to recover the results obtained from a perturbative analysis [60]). However, for large overdensities shell crossing appears at some stage (typically for $\delta_x > 200$), after which Eq.(117) no longer holds [61, 63]. Nevertheless, for lower densities one obtains the asymptotic behaviour $\mathcal{P}(\delta_x) \sim e^{-\delta_{L(\Lambda)}^2 / (2\sigma_{q(\Lambda)}^2)}$. This also determines the large-mass tail of the halo mass function $n(M)dM/M$, where we define halos as spherical objects with a fixed density contrast threshold $\delta = 200$,

$$M \rightarrow \infty : \ln[n(M)] \sim -\frac{\delta_{L(\Lambda)}(M)^2}{2\sigma_{(\Lambda)}(M)^2}, \quad (119)$$

with

$$\delta_{L(\Lambda)}(M) = \mathcal{F}_q^{-1}(\delta), \quad (120)$$

where $\sigma_{(\Lambda)}(M) = \sigma_{q(\Lambda)}$ with $M = \bar{\rho}_m 4\pi q^3/3$.

As in [57, 63], a simple approximation for the mass function that satisfies the large-mass asymptote (119) can be obtained using the Press & Schechter scaling variable ν [67],

$$n(M) \frac{dM}{M} = \frac{\bar{\rho}_m}{M} f(\nu) \frac{d\nu}{\nu} \quad (121)$$

with

$$\nu = \frac{\mathcal{F}_q^{-1}(200)}{\sigma_{(\Lambda)}(M)}, \quad (122)$$

where we choose to define halos by the nonlinear density threshold $\delta = 200$. The scaling function $f(\nu)$ is obtained from a fit to Λ CDM numerical simulations that satisfies the exponential tail $f(\nu) \sim e^{-\nu^2/2}$ [63]

$$f(\nu) = 0.502 [(0.6\nu)^{2.5} + (0.62\nu)^{0.5}] e^{-\nu^2/2}. \quad (123)$$

This ensures that the halo mass function is always normalized to unity and obeys the large-mass tail (119), for any spherical-collapse mapping \mathcal{F}_q . The only change from the Λ CDM cosmology is that the linear threshold $\mathcal{F}_q^{-1}(200)$ in Eq.(122) now depends on the mass M through the scale $q(M)$. The approximation (123) only ensures that the large-mass tail is correct, but it may happen that the low-mass power-law tail should depend on ϵ . An analysis of such effects would require numerical simulations because analytical methods cannot predict the low-mass tail of the halo mass function (which is sensitive to mergers and non-local effects). Nevertheless, we can expect modifications for moderate masses to be less important and partly taken into account through the normalization constraint of the mass function.

As compared with the excursion set approach presented in [59, 68, 69], we do not include screening effects but we take into account the dependence on wavenumber of the modified-gravity kernel $\epsilon(k, a)$. As explained

in Sect. V, this leads to a mass-dependent linear threshold $\delta_L(M)$ whence to deviations from the Λ CDM mass function that will depend on mass.

We show the halo mass function in Fig. 11, and its relative deviation from the Λ CDM mass function in Fig. 12. Here we use the approximation (102) for the mapping $\mathcal{F}_q(\delta_{Lq(\Lambda)})$ but we checked that using Eq.(96) yields close results. For the models that we consider here the mass functions are very close to each other and relative deviations are on the order of 10% or less. In agreement with the behaviour of the probability distribution $\mathcal{P}(\delta_x)$ discussed in the previous section, a positive $\epsilon(k, a)$ leads to more numerous high density fluctuations and to a larger number of massive collapsed halos. This explains why the ratio to the Λ CDM mass function is greater than unity for $\nu > 1$, which corresponds to rare halos. Again, this relative deviation grows for lower n and smaller m_0 .

The same trends appear in numerical simulations of similar modified gravity scenarios [22, 65, 70, 71], with an increase of the large-mass tail for models with an effective amplification of gravity. We show our results for $f(R)$ models with $|f_{R0}| = 10^{-4}, 10^{-5}, 10^{-6}$, as in [22, 70, 71], in Appendix A.

On the mass scales shown in Fig. 12, the ratio keeps growing at high masses for $m_0 = 0.1$ while it decreases for $m_0 = 1$. As in the high-density tail shown in Fig. 10, this is due to two competing effects: i) the exponential tail (119) of the halo mass function amplifies the sensitivity to modified-gravity effects at large masses, but ii) these deviations from General Relativity decrease at large scale whence at large mass ($\epsilon(k, a) \rightarrow 0$ for $k \rightarrow 0$), as seen in Fig. 8. Then, depending on the relative importance of both effects, the ratio of the mass function to its Λ CDM reference may or may not grow with mass on the scales that are considered. As expected, a lower parameter m_0 (which implies a modification of gravity up to larger scales, $k \sim m_0$ and $q \sim 1/m_0$, see Eq.(11)) yields a slower convergence to General Relativity at high mass, whence a larger weight to the first effect i) above. This explains why on the mass scales shown in Fig. 12 the ratio keeps growing at high masses for $m_0 = 0.1$ while it decreases for $m_0 = 1$.

VIII. FROM LINEAR TO HIGHLY NONLINEAR SCALES

Following [32, 40], we can combine the perturbative results of Sect. IV with the halo mass function of Sect. VII to obtain the matter density power spectrum and bispectrum from linear to highly nonlinear scales. As in the usual halo model [72], we write the nonlinear power spectrum as the sum of “two-halo” and “one-halo” terms,

$$P(k) = P_{2H}(k) + P_{1H}(k), \quad (124)$$

where P_{2H} is the contribution from pairs of particles that are located in two different halos and P_{1H} is the contribution from pairs located in the same halo. As explained

in [32], P_{2H} contains the perturbative contribution to the power spectrum and we write

$$P_{2H}(k) = F_{2H}(2\pi/k) P_{\text{pert}}(k), \quad (125)$$

where $F_{2H}(q)$ is the fraction of pairs, with initial (i.e. Lagrangian) separation q , that belong to two distinct halos, and $P_{\text{pert}}(k)$ is the power spectrum obtained by perturbation theory. It is not possible to use the standard one-loop prediction, unless one adds a high- k cutoff, because it grows too fast at high k and leads to unphysical results at high k for the sum (124). Here we consider the one-loop prediction $P_{\text{pert}}(k)$ given by the resummation (68) with Eqs.(66)-(67). Indeed, at this order it yields $P_{\text{pert}}(k) \sim P_L(k)$ at high k [28], so that the two-halo term is subdominant with respect to the one-halo term and one obtains a good match to numerical simulations [32, 40]. Next, the one-halo contribution, which is fully nonperturbative, reads [32]

$$P_{1H}(k) = \int_0^\infty \frac{d\nu}{\nu} f(\nu) \frac{M}{\bar{\rho}_m (2\pi)^3} \left(\tilde{u}_M(k)^2 - \tilde{W}(kq)^2 \right), \quad (126)$$

where \tilde{W} is the Fourier transform of the 3D top-hat, defined in Eq.(90), and \tilde{u}_M is the normalized Fourier transform of the density profile $\rho_M(x)$ of halos of mass M ,

$$\tilde{u}_M(k) = \frac{1}{M} \int d\mathbf{x} e^{-i\mathbf{k}\cdot\mathbf{x}} \rho_M(x). \quad (127)$$

We use the usual “NFW” halo profile [73], with the mass-concentration relation from [32]. Therefore, we do not take into account the effects of the modified gravity on the shape of the profiles of the dark matter halos. Our one-halo term P_{1H} only depends on $\epsilon(k, a)$ through the change of the halo mass function described in Sect. VII. The counterterm \tilde{W}^2 in Eq.(126) ensures that the one-halo contribution decays as $P_{1H}(k) \propto k^2$ at low k , so that the total power (124) converges to the linear power on large scales. This follows from the conservation of matter and the fact that halo formation corresponds to a small-scale redistribution of matter [32, 74] [79].

In a similar fashion, the matter density bispectrum can be written as the sum of three-halo, two-halo, and one-halo terms,

$$B = B_{3H} + B_{2H} + B_{1H}, \quad (128)$$

with [40],

$$B_{3H}(k_1, k_2, k_3) = B_{\text{pert}}(k_1, k_2, k_3), \quad (129)$$

$$B_{2H}(k_1, k_2, k_3) = P_L(k_1) \int \frac{d\nu}{\nu} \frac{M}{\bar{\rho}_m (2\pi)^3} f(\nu) \times \prod_{j=2}^3 \left(\tilde{u}_M(k_j) - \tilde{W}(k_j q) \right) + 2 \text{ cyc.}, \quad (130)$$

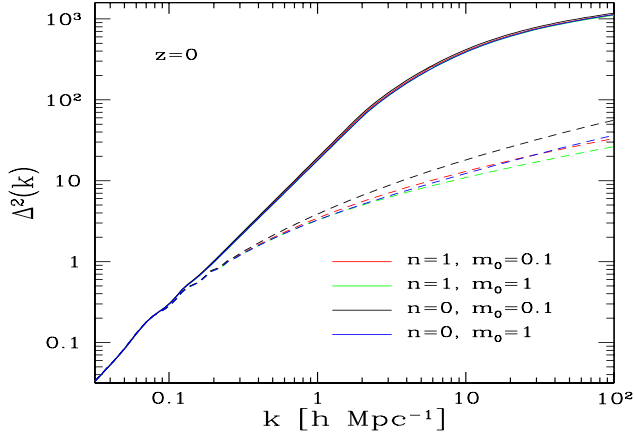


FIG. 13: Logarithmic power, $\Delta^2(k) = 4\pi k^3 P(k)$, at $z = 0$ for four (n, m_0) models. In each case we plot the linear power (dashed line) and the nonlinear power (solid line).

$$B_{1H}(k_1, k_2, k_3) = \int \frac{d\nu}{\nu} f(\nu) \left(\frac{M}{\bar{\rho}_m (2\pi)^3} \right)^3 \times \prod_{j=1}^3 \left(\tilde{u}_M(k_j) - \tilde{W}(k_j q) \right) + 2 \text{ cyc.}, \quad (131)$$

Again, the counterterms \tilde{W} in Eqs.(130) and (131) ensure that the two-halo and one-halo contributions decay on large scales so that the bispectrum converges to the perturbative prediction B_{pert} . As found in [40] and contrary to the situation encountered for the power spectrum, the standard one-loop perturbation theory prediction for B_{pert} is well-behaved at high k (i.e., it is significantly smaller than the one-halo contribution) and it is more accurate than the resummation schemes that have already been studied. Therefore, we only consider the standard perturbative approach for the three-halo contribution (129). More precisely, we use the exact tree-level result (79) and the approximate one-loop correction (80) by setting $B_{\text{pert}} = B^{\text{tree}} + B^{\text{1loop}}$.

While Eq.(128) yields a reasonably good match to numerical simulations ($\sim 10\%$) over all scales for the bispectrum [40], Eq.(124) significantly underestimates the power spectrum on the transition scales (by $\sim 20-30\%$), even though it gives a good accuracy on larger scales ($\sim 1\%$ below $k \simeq 0.3 h \text{ Mpc}^{-1}$ at $z = 1$) and smaller scales ($\sim 10\%$ above $k \simeq 5 h \text{ Mpc}^{-1}$ at $z = 1$). Following [40], we consider a simple power-law interpolation P_{tang} between large and small scales,

$$P_{\text{tang}}(k) = P_{2H+1H}(k) \text{ for } k \leq k_- \text{ and } k \geq k'_+ \quad (132)$$

and

$$P_{\text{tang}}(k) \text{ is a power law within } k_- \leq k \leq k'_+. \quad (133)$$

The transition range $[k_-, k'_+]$ is automatically determined from the shape of $P_{2H+1H}(k)$ and $B(k, k, k)$ and it depends on the shape of the linear power spectrum and

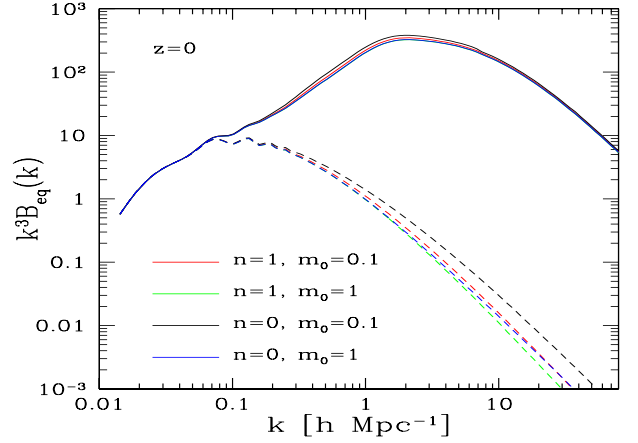


FIG. 14: Equilateral bispectrum $B_{\text{eq}}(k) = B(k, k, k)$, at $z = 0$ for four (n, m_0) models. The bispectrum is multiplied by a factor k^3 in this plot to decrease the range spanned by the vertical axis and to make the figure easier to read. In each case we plot the tree-level bispectrum (dashed line) and the full nonlinear bispectrum (solid line).

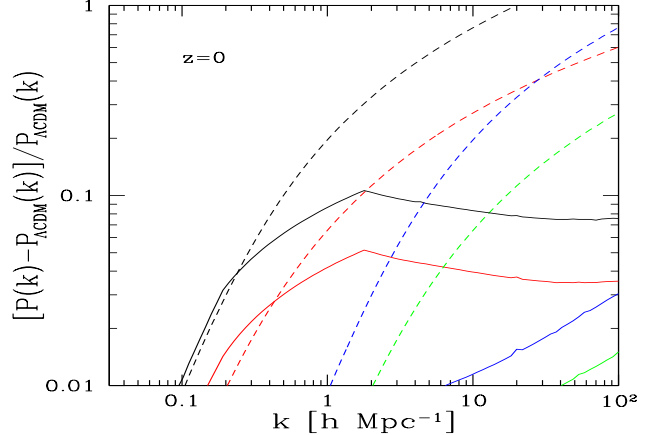


FIG. 15: Relative deviation from ΛCDM of the power spectrum obtained in four models at redshift $z = 0$. In each case, we plot both the relative deviation of the linear power (dashed line) and of the nonlinear power (solid line). From left to right we consider the models $(n, m_0) = (0, 0.1), (1, 0.1), (0, 1)$, and $(1, 1)$.

on redshift. This improves the agreement with numerical simulations in the ΛCDM cosmology [40] while keeping the perturbative and 1-halo behaviours on large and small scales.

We show in Figs. 13 and 14 the matter density power spectrum and bispectrum that we obtain at redshift $z = 0$, from linear to highly nonlinear scales. The various curves are very close and we can see that at high k the deviations are actually damped by nonlinear effects. Within our framework, this is because we ne-

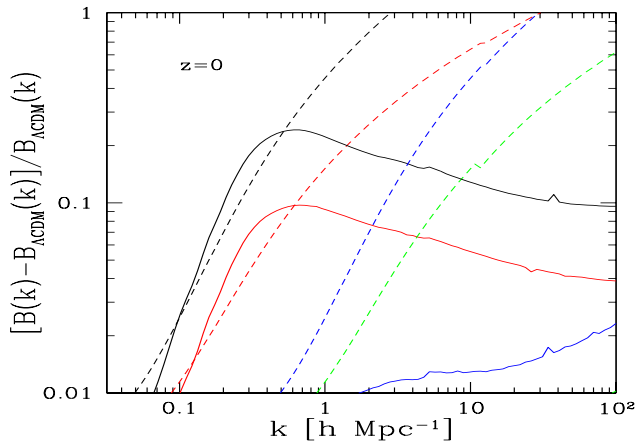


FIG. 16: Relative deviation from Λ CDM of the bispectrum obtained in four models at redshift $z = 0$. In each case, we plot both the relative deviation of the tree-level bispectrum (dashed line) and of the nonlinear bispectrum (solid line). From left to right we consider the models $(n, m_0) = (0, 0.1), (1, 0.1), (0, 1),$ and $(1, 1)$.

glected any impact of modified gravity on the halo profile (127) and the only influence of modified gravity appears through the halo mass function $n(M)$. This may not be such a bad approximation because in more realistic models modifications to gravity vanish on small scales (e.g., through chameleon or Vainshtein mechanisms) so that the density profiles of small halos are expected to converge to the GR behaviour. Then, we expect that our modelization provides a similar accuracy to the one found in Λ CDM cosmology by comparison with numerical simulations [32, 40]. As in Sect. IV D, we clearly see that nonlinear gravitational clustering amplifies both the power spectrum and bispectrum at high k but damps the baryon acoustic oscillations. As in [32, 40], our approach allows us to describe the power spectrum and bispectrum from large linear scales down to small highly nonlinear scales.

We show in Figs. 15 and 16 the relative deviations from the Λ CDM reference of the power spectrum and of the equilateral bispectrum. In the weakly nonlinear regime the relative deviations grow with k , following the behaviour of $\epsilon(k, a)$. In agreement with the discussions above, they reach a maximum on transition scales, starting to deviate from the Λ CDM growth for $k \sim m_0$, and then slowly declining on highly nonlinear scales. On these nonlinear scales, the relative deviations at the level of the linear or tree-order contributions are no longer a good estimate of the actual signal and greatly overestimate the effects of modified gravity. Since the theoretical accuracy is greater on weakly nonlinear scales (which can be analyzed by systematic perturbative approaches) than on highly nonlinear scales (which require phenomenological ingredients such as halo profiles), these behaviours suggest that it is more efficient to focus on weakly nonlinear

scales to probe such modifications of gravity.

It is also worth emphasizing that the deviations from Λ CDM which we have calculated with the steepest descent resummation method together with the halo model show the same trends as the N-body results [22, 23] obtained for models with $n = 1$ and $|f_{R0}| = 10^{-4}, 10^{-5}, 10^{-6}$. Indeed, numerical results show that the deviation from Λ -CDM reaches a peak at weakly nonlinear scales before decreasing on highly nonlinear scales. Simple fitting procedures designed for Λ CDM cosmology [75] have been shown not to provide good results and to miss this high- k behavior [23]. This shows the advantage of approaches like ours that are closer to physical modeling. Even though they may be less accurate than a specific fitting formula, their behaviour as cosmological parameters and scenarios are modified is more reliable.

IX. CONCLUSION

We have considered the dynamics of structure formation in modified gravity models analytically. To do so, we have used a steepest descent technique for the generating functional of density and velocity perturbations as well as the spherical collapse dynamics. The models we have considered correspond to screened modifications of gravity due to a scalar field. In numerical examples we have focused on models defined by a power law mass function and a constant coupling to matter, which coincide with $f(R)$ models in the large curvature limit and in the matter era, although the techniques developed here are general. The results we have presented comprise the power spectrum, the bispectrum, the probability distribution of the density contrast, and the large-mass tail of the halo mass function. Modified gravity has interesting features astrophysically when the ratio of the mass of the scalar field over the Hubble rate now m_0/H_0 is of order 10^3 . In this case, deviations can be substantial and larger than a few percent. In this paper, we do not attempt to give precise predictions, we are more interested in indications that can be obtained relatively fast using our analytical tools without the need for large N-body simulations.

After a description of the linear growing and decaying modes, which become k -dependent in these modified-gravity scenarios, we have obtained the associated linear growth rate $f(k, z)$. For the realistic parameters (n, m_0) studied here measuring its deviation from the General Relativity prediction remains challenging, but future surveys such as Euclid should give a clear signal for the most favorable cases (e.g., $(n, m_0) = (0, 0.1)$).

Next, we have described how higher-order perturbative contributions can be computed in the weakly nonlinear regime. The dependence on wavenumber of the linear modes makes numerical implementations of these perturbative schemes significantly more complex than in the usual General Relativity case, because time- and scale-dependences no longer factor out. We have pre-

sented the generalization of the “standard” perturbative approach as well as a “steepest descent” approach that performs partial resummations of higher-order diagrams. The path-integral formalism that underlies this second method also provides an efficient route to recover the standard perturbative approach and avoids the need to compute the n -point kernels F_n^s . We find that for realistic modified-gravity scenarios, such as the ones investigated here, the deviations of the power spectrum from General Relativity on BAO scales are quite modest (typically less than 6%) and below the accuracy of the standard perturbative approach at one-loop order. This means that one must use more accurate schemes, such as the one-loop steepest-descent approach presented here, or possibly include higher-order terms within the standard approach (but its convergence is not very well behaved).

For the bispectrum we find that nonperturbative contributions (associated with one-halo and two-halo terms) cannot be neglected on the weakly nonlinear scales where the deviations from General Relativity can be detected. This suggests that for practical purposes the power spectrum is a more reliable probe of such modified-gravity effects, because its deviations from the GR predictions are larger than for the bispectrum in the perturbative regime, where rigorous and systematic approaches can be developed.

To go beyond these low-order perturbative approaches, we have described the dynamics of spherical density fluctuations, which can be exactly solved before shell crossing. Again, modifications to gravity make the analysis significantly more complex, because the motions of different shells no longer decouple, even before any shell crossing. This means that one must solve the evolution with time of the full density profile. Nevertheless, we have introduced a simple approximation for typical profiles that allows to decouple the motion of the mass shell of interest. We find this provides a reasonable approximation to the exact dynamics (but slightly underestimates the effects of modified gravity). This analysis provides the characteristic dependence on mass of the critical linear density threshold $\delta_c(M)$ associated with a given nonlinear threshold (such as $\delta = 200$). In the cases studies here, where the function $\epsilon(k, a)$ is positive and corresponds to a time- and scale-dependent effective amplification of gravity, this threshold $\delta_c(M)$ decreases at low mass (because this amplification is larger on smaller scales) and converges to the constant GR prediction at large mass (because we recover General Relativity on large scales).

In contrast to some previous works, this dependence on mass does not arise from screening effects (that depend on mass through the depth of the gravitational potential, which triggers the screening mechanism) but from the k -dependence of the modified-gravity kernel $\epsilon(k, a)$.

This also allows us to obtain the probability distribution, $\mathcal{P}(\delta_x)$, of the nonlinear density contrast within spherical cells, in the weakly nonlinear regime. Because of this effective amplification of gravity, the tails of $\mathcal{P}(\delta_x)$ grow with respect to the General Relativity prediction

(and by conservation of the probability normalization to unity $\mathcal{P}(\delta_x)$ decreases for moderate density fluctuations). This growth is smaller and the relative ratio to GR does not necessarily goes to infinity in the large-density tail, as opposed to the low-density tail, because on large scale the dynamics converges to General Relativity.

The same effect amplifies the large-mass tail of the halo mass function. Again, the ratio to the GR prediction may increase or decrease with mass in the range of interest depending on how fast modifications to gravity vanish on large scales.

Finally, combining perturbative approaches with halo models, we have computed a simple estimate of the power spectrum and bispectrum from linear to highly nonlinear scales. Within this modelisation, we find that the relative deviation from General Relativity is the largest on the transition scales between the linear and the highly nonlinear regimes, for both the power spectrum and bispectrum. Since nonlinear scales are difficult to predict with a high accuracy (because of the complex nonperturbative dynamics associated with shell crossings and because one should include baryon and galaxy formation effects), this suggests that weakly nonlinear scales, in particular in the perturbative regime, are the best probes of these modified-gravity models.

Our methods call for improvements to reach the needs of precision cosmology. Indeed we have neglected, for ease of treatment and as a first step, two major effects. The first one consists in including non-linearities in the scalar field sector of the models. Here the scalar field dynamics are only linear and non-linear effects in both the potential and the coupling to matter ought to be considered. Technically, this can be done at the one loop level by self-consistently modifying the Euler equation with non-linear terms coming from the scalar field interaction with matter particles. A second ingredient we have not considered so far is the screening of the scalar force in dense environments. This will modify the spherical collapse of over densities and therefore the halo statistics. Eventually this will have an impact on the growth of non-linear structures. As a result, the effects described in this paper can only be taken as indications on quasi-linear scales. Work on all these aspects is in progress. We also intend to carry out a comparison of our analytical results with the N-body simulations which use the same mass and coupling parameterisation of modified gravity. Doing so, and for a greater variety of models including dilatons and symmetrons, we hope to validate our analytical approach which could then be used for models that will appear in the future and be analysed without the need for large N-body simulations.

Appendix A: The case of $f(R)$ models

We consider in this appendix the case of $f(R)$ models which have also been studied through numerical simulations, with a power-law form as in Eq.(16). The mass of

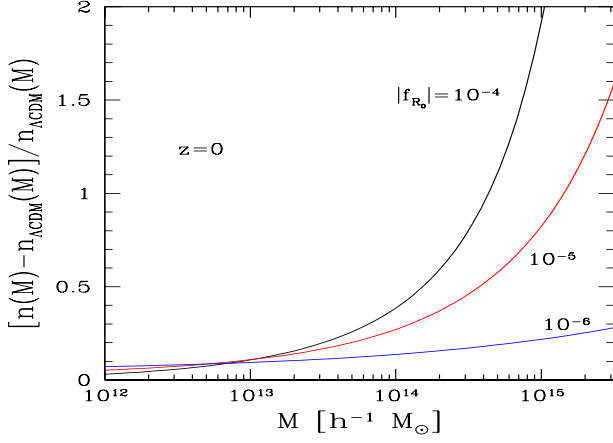


FIG. 17: Relative deviation from Λ CDM of the halo mass function at redshift $z = 0$, for $n = 1$ and $|f_{R_0}| = 10^{-4}, 10^{-5}$, and 10^{-6} , from top to bottom.

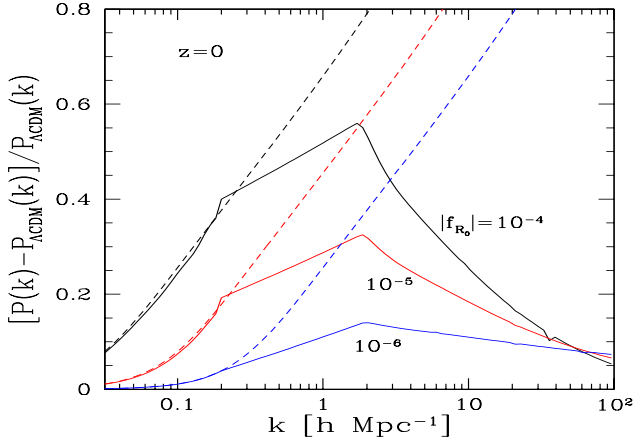


FIG. 18: Relative deviation from Λ CDM of the power spectrum at redshift $z = 0$, for $n = 1$ and $|f_{R_0}| = 10^{-4}, 10^{-5}$, and 10^{-6} . In each case, we plot both the relative deviation of the linear power (dashed line) and of the nonlinear power (solid line).

the scalar field evolves with time as [23]

$$m(a) = m_0 \left(\frac{\Omega_{m0}(1+z)^3 + 4\Omega_{\Lambda0}}{\Omega_{m0} + 4\Omega_{\Lambda0}} \right)^{(n+2)/2}, \quad (\text{A1})$$

where m_0 is given by Eq.(17). This gives the approximate scaling (15) at high redshift but for accurate computations it is necessary to use the more precise expression (A1).

To compare with the numerical results of [22, 23, 70, 71] we adopt the same WMAP3 Λ CDM reference model [76], with cosmological parameters $(\Omega_m, \Omega_b, h, \sigma_8, n_s) = (0.24, 0.04181, 0.73, 0.76, 0.958)$. We focus on the case

$n = 1$, with the amplitudes $|f_{R_0}| = 10^{-4}, 10^{-5}$, and 10^{-6} . We show in Figs. 17, 18, and 19, the relative deviations

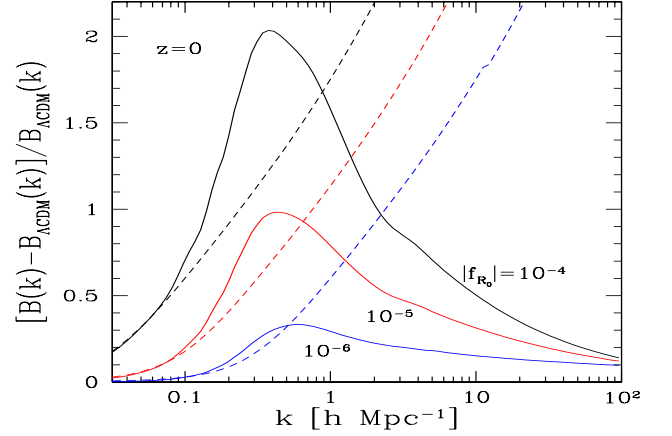


FIG. 19: Relative deviation from Λ CDM of the bispectrum at redshift $z = 0$, for $n = 1$ and $|f_{R_0}| = 10^{-4}, 10^{-5}$, and 10^{-6} . In each case, we plot both the relative deviation of the tree-level bispectrum (dashed line) and of the nonlinear bispectrum (solid line).

from the Λ CDM reference of the halo mass function, the matter power spectrum, and the bispectrum. Our results are similar to the ones obtained in Figs. 12, 15, and 16, in the main text, for our power-law models parameterized by (n, m_0) . We can check that our results also show a reasonable agreement with the “no-chameleon” numerical simulations of [22, 23, 70, 71] for the halo mass function and the power spectrum, although we may overestimate the large-mass tail for $M > 10^{15} h^{-1} M_\odot$. The almost straight lines on transition scales in Fig. 18 correspond to the interpolation (133) and should not be considered as an accurate prediction. However, they correctly reproduce the saturation of the relative deviation and the transition towards the highly nonlinear regime (dominated by the one-halo contribution) where the relative deviation declines (within our framework, where we neglect modifications of halo profiles). The same behavior is found in numerical simulations [23], with a reasonably good quantitative match. It is interesting to note that using simple fitting procedures designed for Λ CDM cosmology, such as the halo-fit from [75], has been shown not to provide good results and to miss this high- k behavior [23]. This is not fully surprising, since such fitting formulae were not designed for these scenarios. This shows the advantage of using approaches such as the one presented in this paper that are closer to physical modeling (using both systematic perturbative expansions and phenomenological halo models). Even though they may be less accurate than a specific fitting formula for the class of models the latter was built from, their behaviour as cosmological parameters and scenarios are modified is more reliable.

-
- [1] E. J. Copeland, M. Sami, and S. Tsujikawa, *Int.J.Mod.Phys.* **D15**, 1753 (2006), hep-th/0603057.
- [2] T. Clifton, P. G. Ferreira, A. Padilla, and C. Skordis, *Phys.Rept.* **513**, 1 (2012), 1106.2476.
- [3] S. Weinberg, *Phys.Rev.* **138**, B988 (1965).
- [4] C. Hoyle, D. Kapner, B. R. Heckel, E. Adelberger, J. Gundlach, et al., *Phys.Rev.* **D70**, 042004 (2004), hep-ph/0405262.
- [5] B. Bertotti, L. Iess, and P. Tortora, *Nature* **425**, 374 (2003).
- [6] J. Khoury (2010), 1011.5909.
- [7] J. Khoury and A. Weltman, *Phys.Rev.Lett.* **93**, 171104 (2004), astro-ph/0309300.
- [8] J. Khoury and A. Weltman, *Phys.Rev.* **D69**, 044026 (2004), astro-ph/0309411.
- [9] P. Brax, C. van de Bruck, A.-C. Davis, J. Khoury, and A. Weltman, *Phys.Rev.* **D70**, 123518 (2004), astro-ph/0408415.
- [10] T. Damour and A. M. Polyakov, *Nucl.Phys.* **B423**, 532 (1994), hep-th/9401069.
- [11] P. Brax, C. van de Bruck, A.-C. Davis, B. Li, and D. J. Shaw, *Phys.Rev.* **D83**, 104026 (2011), 1102.3692.
- [12] P. Brax, C. van de Bruck, A.-C. Davis, and D. Shaw, *Phys.Rev.* **D82**, 063519 (2010), 1005.3735.
- [13] A. Nicolis, R. Rattazzi, and E. Trincherini, *Phys.Rev.* **D79**, 064036 (2009), 0811.2197.
- [14] M. Pietroni, *Phys.Rev.* **D72**, 043535 (2005), astro-ph/0505615.
- [15] K. A. Olive and M. Pospelov, *Phys.Rev.* **D77**, 043524 (2008), 0709.3825.
- [16] K. Hinterbichler and J. Khoury, *Phys.Rev.Lett.* **104**, 231301 (2010), 1001.4525.
- [17] P. Brax, A.-C. Davis, B. Li, and H. A. Winther (2012), 1203.4812.
- [18] P. Brax, C. van de Bruck, A.-C. Davis, and A. M. Green, *Phys.Lett.* **B633**, 441 (2006), astro-ph/0509878.
- [19] F. Bernardeau and P. Brax, *JCAP* **6**, 19 (2011), 1102.1907.
- [20] P. Brax, R. Rosenfeld, and D. Steer, *JCAP* **1008**, 033 (2010), 1005.2051.
- [21] B. Li and G. Efstathiou (2011), 1110.6440.
- [22] F. Schmidt, M. Lima, H. Oyaizu, and W. Hu, *Phys. Rev. D* **79**, 083518 (2009), 0812.0545.
- [23] H. Oyaizu, M. Lima, and W. Hu, *Phys. Rev. D* **78**, 123524 (2008), 0807.2462.
- [24] H. Gil-Marin, F. Schmidt, W. Hu, R. Jimenez, and L. Verde, *JCAP* **1111**, 019 (2011), 1109.2115.
- [25] W. Hu and I. Sawicki, *Phys.Rev.* **D76**, 064004 (2007), 0705.1158.
- [26] P. Brax, A.-C. Davis, and B. Li (2011), 1111.6613.
- [27] M. Crocce and R. Scoccimarro, *Phys. Rev. D* **73**, 063519 (2006), arXiv:astro-ph/0509418.
- [28] P. Valageas, *Astr. & Astrophys.* **465**, 725 (2007), arXiv:astro-ph/0611849.
- [29] A. Taruya and T. Hiramatsu, *Astrophys. J.* **674**, 617 (2008), 0708.1367.
- [30] M. Pietroni, *JCAP* **10**, 36 (2008), 0806.0971.
- [31] P. Valageas, *Astr. & Astrophys.* **476**, 31 (2007), 0706.2593.
- [32] P. Valageas and T. Nishimichi, *Astr. & Astrophys.* **527**, A87+ (2011), 1009.0597.
- [33] F. Bernardeau, S. Colombi, E. Gaztañaga, and R. Scoccimarro, *Phys. Rep.* **367**, 1 (2002), arXiv:astro-ph/0112551.
- [34] R. Laureijs, J. Amiaux, S. Arduini, J. . Auguères, J. Brinchmann, R. Cole, M. Cropper, C. Dabin, L. Duvet, A. Ealet, et al., arXiv:1110.3193L (2011), 1110.3193.
- [35] P. Valageas, *Astr. & Astrophys.* **484**, 79 (2008), 0711.3407.
- [36] M. H. Goroff, B. Grinstein, S.-J. Rey, and M. B. Wise, *Astrophys. J.* **311**, 6 (1986).
- [37] P. J. E. Peebles, *The large-scale structure of the universe* (Princeton University Press, Princeton, N.J., USA, 1980).
- [38] P. C. Martin, E. D. Siggia, and H. A. Rose, *Phys. Rev. A* **8**, 423 (1973).
- [39] R. Phythian, *Journal of Physics A Mathematical General* **10**, 777 (1977).
- [40] P. Valageas and T. Nishimichi, *Astr. & Astrophys.* **532**, A4+ (2011), 1102.0641.
- [41] P. Valageas, *Astr. & Astrophys.* **421**, 23 (2004), arXiv:astro-ph/0307008.
- [42] J. Zinn-Justin, *Quantum field theory and critical phenomena* (Oxford: Clarendon Press, 1989).
- [43] K. Koyama, A. Taruya, and T. Hiramatsu, *Phys. Rev. D* **79**, 123512 (2009), 0902.0618.
- [44] M. Crocce and R. Scoccimarro, *Phys. Rev. D* **73**, 063520 (2006), arXiv:astro-ph/0509419.
- [45] F. Bernardeau and P. Valageas, *Phys. Rev. D* **81**, 043516 (2010), 0912.0356.
- [46] F. Bernardeau and P. Valageas, *Phys. Rev. D* **85**, 023516 (2012), 1109.4223.
- [47] F. Bernardeau, M. Crocce, and R. Scoccimarro, *Phys. Rev. D* **78**, 103521 (2008), 0806.2334.
- [48] F. Bernardeau, N. van de Rijt, and F. Vernizzi, *Phys. Rev. D* **85**, 063509 (2012), 1109.3400.
- [49] S. Anselmi and M. Pietroni, *ArXiv e-prints* (2012), 1205.2235.
- [50] S. Matarrese and M. Pietroni, *Modern Physics Letters A* **23**, 25 (2008), arXiv:astro-ph/0702653.
- [51] T. Matsubara, *Phys. Rev. D* **77**, 063530 (2008), 0711.2521.
- [52] D. J. Eisenstein, W. Hu, and M. Tegmark, *Astrophys. J.* **518**, 2 (1999), arXiv:astro-ph/9807130.
- [53] E. Sefusatti, M. Crocce, S. Pueblas, and R. Scoccimarro, *Phys. Rev. D* **74**, 023522 (2006), arXiv:astro-ph/0604505.
- [54] E. Komatsu, J. Dunkley, M. R. Nolta, C. L. Bennett, B. Gold, G. Hinshaw, N. Jarosik, D. Larson, M. Limon, L. Page, et al., *Astrophys. J. Suppl. Ser.* **180**, 330 (2009), 0803.0547.
- [55] A. Lewis, A. Challinor, and A. Lasenby, *Astrophys. J.* **538**, 473 (2000), arXiv:astro-ph/9911177.
- [56] D. J. Eisenstein, I. Zehavi, D. W. Hogg, R. Scoccimarro, M. R. Blanton, R. C. Nichol, R. Scranton, H.-J. Seo, M. Tegmark, Z. Zheng, et al., *Astrophys. J.* **633**, 560 (2005), arXiv:astro-ph/0501171.
- [57] P. Valageas, *Astr. & Astrophys.* **514**, A46+ (2010), 0906.1042.
- [58] L. Wang and P. J. Steinhardt, *Astrophys. J.* **508**, 483 (1998), arXiv:astro-ph/9804015.
- [59] B. Li and G. Efstathiou, *Mon. Not. R. Astr. Soc.* **421**,

- 1431 (2012), 1110.6440.
- [60] F. Bernardeau, *Astrophys. J.* **427**, 51 (1994), arXiv:astro-ph/9311066.
 - [61] P. Valageas, *Astr. & Astrophys.* **382**, 450 (2002), arXiv:astro-ph/0107333.
 - [62] P. Valageas, *Astr. & Astrophys.* **382**, 412 (2002), arXiv:astro-ph/0107126.
 - [63] P. Valageas, *Astr. & Astrophys.* **508**, 93 (2009), 0905.2277.
 - [64] F. Bernardeau, *Astr. & Astrophys.* **291**, 697 (1994), arXiv:astro-ph/9403020.
 - [65] W. A. Hellwing and R. Juszkiewicz, *Phys. Rev. D* **80**, 083522 (2009), 0809.1976.
 - [66] B. Li, G.-B. Zhao, and K. Koyama, *Mon. Not. R. Astr. Soc.* **421**, 3481 (2012), 1111.2602.
 - [67] W. H. Press and P. Schechter, *Astrophys. J.* **187**, 425 (1974).
 - [68] B. Li and T. Y. Lam, ArXiv e-prints (2012), 1205.0058.
 - [69] T. Y. Lam and B. Li, ArXiv e-prints (2012), 1205.0059.
 - [70] Y. Li and W. Hu, *Phys. Rev. D* **84**, 084033 (2011), 1107.5120.
 - [71] S. Ferraro, F. Schmidt, and W. Hu, *Phys. Rev. D* **83**, 063503 (2011), 1011.0992.
 - [72] A. Cooray and R. Sheth, *Phys. Rep.* **372**, 1 (2002), astro-ph/0206508.
 - [73] J. F. Navarro, C. S. Frenk, and S. D. M. White, *Astrophys. J.* **490**, 493 (1997), arXiv:astro-ph/9611107.
 - [74] P. J. E. Peebles, *Astr. & Astrophys.* **32**, 391 (1974).
 - [75] R. E. Smith, J. A. Peacock, A. Jenkins, S. D. M. White, C. S. Frenk, F. R. Pearce, P. A. Thomas, G. Efstathiou, and H. M. P. Couchman, *Mon. Not. R. Astr. Soc.* **341**, 1311 (2003), arXiv:astro-ph/0207664.
 - [76] D. N. Spergel, R. Bean, O. Doré, M. R. Nolta, C. L. Bennett, J. Dunkley, G. Hinshaw, N. Jarosik, E. Komatsu, L. Page, et al., *Astrophys. J. Suppl. Ser.* **170**, 377 (2007), arXiv:astro-ph/0603449.
 - [77] Although the result at each order P_{L0}^n , or $K_s^{2(n-1)}$, is identical whether one uses either of these two methods, this term of order n is split in different manners in the two methods as they involve different types of diagrams, see [35] for details.
 - [78] In the context of Λ CDM cosmologies, this feature appears for power-law initial power spectra $P_L(k) \propto k^n$ with $n < 0$, see [62] for details.
 - [79] Taking into account momentum conservation would give an even steeper k^4 tail [74] but the form (126) is sufficient for practical purposes.